Supporting Information

Title: Modular Self-Assembly of Protein Cage Lattices for Multistep Catalysis

Authors: Masaki Uchida[1], Kimberly McCoy[1], Masafumi Fukuto[2,3], Lin Yang[2], Hideyuki Yoshimura[1,4], Heini M. Miettinen[5], Ben LaFrance[6], Dustin P. Patterson[7], Benjamin Schwarz[1], Jonathan A. Karty[1], Peter E. Prevelige Jr. [8], Byeongdu Lee[9]*, Trevor Douglas[1]*

Affiliations:
1. Department of Chemistry, Indiana University, 800 East Kirkwood Ave., Bloomington, IN 47405, USA
2. National Synchrotron Light Source II, Brookhaven National Laboratory, Upton, NY 11973, USA
3. Condensed Matter Physics and Materials Science Department, Brookhaven National Laboratory, Upton, NY 11973, USA
4. Department of Physics, Meiji University, 1-1-1 Higashimita, Tama-ku, Kawasaki, 214-8571, Japan
5. Department of Microbiology and Immunology, Montana State University, Bozeman, Montana 59717, USA
6. Department of Chemistry and Biochemistry, Montana State University, Bozeman, Montana 59717, USA
7. Department of Chemistry and Biochemistry, University of Texas at Tyler, Tyler, Texas 75799, USA
8. Department of Microbiology, University of Alabama at Birmingham, Birmingham, Alabama 35294, USA
9. X-ray science division, Advanced Photon Source, Argonne National Laboratory, 9700 South Cass Ave., Argonne, IL 60439, USA

* Corresponding author:
Trevor Douglas
Department of Chemistry, Indiana University
800 East Kirkwood Ave., Bloomington, IN 47405
Phone: (812)-856-6936
Fax: (812)-856-5710
Email: trevdoug@indiana.edu

Byeongdu Lee
X-ray science division, Advanced Photon Source, Argonne National Laboratory
9700 South Cass Ave., Argonne, IL 60439
Phone: (630)-252-0395
Email: blee@aps.anl.gov

Table of Contents

Section 1. DNA sequences of proteins used in this study

CP

ATG GCT TTG AAC GAA GGT CAA ATT GTT ACA CTG GCG GTA GAT GAA ATC ATC GAA ACC ATC TCC GCA
ATC ACT CCA ATG GCG CAG AAA GCC AAG AAA TAC ACC CCG CCT GCT GCT TGT ATG CAG CGC TCC AGC
AAT ACC ATC TGG ATG CCT GTA GAG CAA GAG TCA CCC ACT CAG GAG GGC TGG GAT TTA ACT GAT AAA
GCG ACA GGG TTA CTG GAA CTT AAC GTC GCG GTA AAC ATG GGA GAG CCG GAT AAC GAC TTC TTC CAG
TTG CGT GCT GAT GAC TTG CGA GAC GAA ACT GCG TAT CGT CGC CGC ATC CAG TCT GCC GCT CGC AAG
CTG GCG AAC AAC GTT GAG TTG AAA GTC GCA AAC ATG GCC GCC GAG ATG GGT TCG CTG GTT ATC ACC
TCC CCT GAT GCC ATC GGC ACT AAT ACC GCA GAC GCC TGG AAC TTT GTG GCC GAC GCA GAA GAA ATC
ATG TTC TCC CGC GAA CTT AAC CGC GAC ATG GGG ACA TCG TAC TTC TTC AAC CCT CAG GAC TAC AAA
AAA GCG GGT TAC GAC CTG ACC AAG CGT GAC ATC TTC GGG CGT ATT CCT GAA GAA GCA TAC CGA GAT
GGC ACC ATT CAG CGT CAG GTC GCT GGC TTC GAT GAT GTC CTG CGC TCT CCG AAA CTT CCT GTG CTG
ACC AAA TCC ACC GCA ACT GGC ATC ACT GTA TCC GGT GCG CAG TCC TTC AAG CCT GTC GCA TGG CAA
CTG GAT AAC GAT GGC AAC AAA GTT AAC GTT GAT AAC CGT TTT GCT ACC GTC ACC CTG TCT GCA ACT
ACC GGC ATG AAA CGC GGC GAC AAA ATT TCG TTT GCT GGC GTT AAG TTC CTT GGT CAG ATG GCT AAG
AAC GTA CTG GCT CAG GAT GCG ACT TTC TCC GTA GTC CGC GTT GTT GAC GGT ACT CAT GTT GAA ATC
ACG CCG AAG CCG GTA GCG CTG GAT GAT GTT TCC CTG TCT CCG GAG CAG CGT GCC TAC GCC AAC GTT
AAC ACC TCG CTG GCT GAT GCA ATG GCA GTG AAC ATT CTG AAC GTT AAA GAC GCT CGC ACT AAT GTG
TTC TGG GCT GAC GAT GCT ATT CGT ATC GTG TCT CAG CCG ATT CCG GCT AAC CAT GAA CTT TTT GCA
GGT ATG AAA ACT ACC TCA TTC AGC ATC CCT GAT GTT GGC CTG AAC GGT ATC TTC GCT ACG CAG GGT
GAT ATT TCC ACC CTG TCC GGC CTG TGC CGT ATT GCG CTG TGG TAC GGC GTA AAC GCG ACA CGA CCG
GAG GCA ATC GGT GTT GGC CTG CCT GGT CAG ACT GCG TAA

CP with E2 (CP-E2)

ATG GCT TTG AAC GAA GGT CAA ATT GTT ACA CTG GCG GTA GAT GAA ATC ATC GAA ACC ATC TCC GCA
ATC ACT CCA ATG GCG CAG AAA GCC AAG AAA TAC ACC CCG CCT GCT GCT TCT ATG CAG CGC TCC AGC
AAT ACC ATC TGG ATG CCT GTA GAG CAA GAG TCA CCC ACT CAG GAG GGC TGG GAT TTA ACT GAT AAA
GCG ACA GGG TTA CTG GAA CTT AAC GTC GCG GTA AAC ATG GGA GAG CCG GAT AAC GAC TTC TTC CAG
TTG CGT GCT GAT GAC TTG CGA GAC GAA ACT GCG TAT CGT CGC CGC ATC CAG TCT GCC GCT CGC AAG
CTG GCG AAC AAC GTT GAG TTG AAA GTC GCA AAC ATG GCC GCC GAG ATG GGT TCG CTG GTT ATC ACC
TCC CCT GAT GCC ATC GGC ACT AAT ACC GCA GAC GCC TGG AAC TTT GTG GCC GAC GCA GAA GAA ATC
ATG TTC TCC CGC GAA CTT AAC CGC GAC ATG GGG ACA TCG TAC TTC TTC AAC CCT CAG GAC TAC AAA
AAA GCG GGT TAC GAC CTG ACC AAG CGT GAC ATC TTC GGG CGT ATT CCT GAA GAA GCA TAC CGA GAT
GGC ACC ATT CAG CGT CAG GTC GCT GGC TTC GAT GAT GTC CTG CGC TCT CCG AAA CTT CCT GTG CTG
ACC AAA TCC ACC GCA ACT GGC ATC ACT GTA TCC GGT GCG CAG TCC TTC AAG CCT GTC GCA TGG CAA
CTG GAT AAC GAT GGC AAC AAA GTT AAC GTT GAT AAC CGT TTT GCT ACC GTC ACC CTG TCT GCA ACT
ACC GGC ATG AAA CGC GGC GAC AAA ATT TCG TTT GCT GGC GTT AAG TTC CTT GGT CAG ATG GCT AAG
AAC GTA CTG GCT CAG GAT GCG ACT TTC TCC GTA GTC CGC GTT GTT GAC GGT ACT CAT GTT GAA ATC
ACG CCG AAG CCG GTA GCG CTG GAT GAT GTT TCC CTG TCT CCG GAG CAG CGT GCC TAC GCC AAC GTT

AAC ACC TCG CTG GCT GAT GCA ATG GCA GTG AAC ATT CTG AAC GTT AAA GAC GCT CGC ACT AAT GTG
TTC TGG GCT GAC GAT GCT ATT CGT ATC GTG TCT CAG CCG ATT CCG GCT AAC CAT GAA CTT TTT GCA
GGT ATG AAA ACT ACC TCA TTC AGC ATC CCT GAT GTT GGC CTG AAC GGT ATC TTC GCT ACG CAG GGT
GAT ATT TCC ACC CTG TCC GGC CTG TGC CGT ATT GCG CTG TGG TAC GGC GTA AAC GCG ACA CGA CCG
GAG GCA ATC GGT GTT GGC CTG CCT GGT CAG ACT GCG ACT AGT GTG GCG GCG CTG GAA AAA GAA GTT
GCC GCC TTG GAG AAG GAG TAG

SP_{141}

ATG GGC AGC AGC CAT CAC CAT CAT CAC CAC AGC CAG GAT CCC TGG TGC CGC GCG GCA GCA TGT CGC
AGC AAT GCC GTA GCA GAA CAG GGC CGC AAG ACT CAG GAG TTT ACC CAG CAA TCA GCG CAA TAC GTC
GAA GCT GCC CGC AAA CAC TAT GAC GCG GCG GAA AAG CTC AAC ATC CCT GAC TAT CAG GAG AAA GAA
GAC GCA TTT ATG CAA CTG GTT CCG CCT GCG GTT GGG GCC GAC ATT ATG CGC CTG TTC CCG GAA AAG
TCC GCC GCG CTC ATG TAT CAC CTG GGG GCA AAC CCG GAG AAA GCC CGC CAG TTA CTG GCG ATG GAT
GGG CAG TCC GCG CTG ATT GAA CTC ACT CGA CTA TCC GAA CGC TTA ACT CTC AAG CCT CGC GGT AAA
CAA ATC TCT TCC GCT CCC CAT GCT GAC CAG CCT ATT ACC GGT GAT GTC AGC GCA GCA AAT AAA GAT
GCC ATT CGT AAA CAA ATG GAT GCT GCT GCG AGC AAG GGA GAT GTG GAA ACC TAC CGC AAG CTA AAG
GCA AAA CTT AAA GGA ATC CGA TAA

KivD-SP_{141}

ATG GCA TAT ACA GTA GGA GAT TAC CTA TTA GAC CGA TTA CAC GAG TTA GGA ATT GAA GAA ATT TTT
GGA GTC CCT GGA GAC TAT AAC TTA CAA TTT TTA GAT CAA ATT ATT TCC CGC AAG GAT ATG AAA TGG
GTC GGA AAT GCT AAT GAA TTA AAT GCT TCA TAT ATG GCT GAT GGC TAT GCT CGT ACT AAA AAA GCT
GCC GCA TTT CTT ACA ACC TTT GGA GTA GGT GAA TTG AGT GCA GTT AAT GGA TTA GCA GGA AGT TAC
GCC GAA AAT TTA CCA GTA GTA GAA ATA GTG GGA TCA CCT ACA TCA AAA GTT CAA AAT GAA GGA AAA
TTT GTT CAT CAT ACG CTG GCT GAC GGT GAT TTT AAA CAC TTT ATG AAA ATG CAC GAA CCT GTT ACA
GCA GCT CGA ACT TTA CTG ACA GCA GAA AAT GCA ACC GTT GAA ATT GAC CGA GTA CTT TCT GCA CTA
TTA AAA GAA AGA AAA CCT GTC TAT ATC AAC TTA CCA GTT GAT GTT GCT GCT GCA AAA GCA GAG AAA
CCC TCA CTC CCT TTG AAA AAA GAA AAC TCA ACT TCA AAT ACA AGT GAC CAA GAG ATC TTG AAC AAA
ATT CAA GAA AGC TTG AAA AAT GCC AAA AAA CCA ATC GTG ATT ACA GGA CAT GAA ATA ATT AGT TTT
GGC TTA GAA AAA ACA GTC TCT CAA TTT ATT TCA AAG ACA AAA CTA CCT ATT ACG ACA TTA AAC TTT
GGA AAA AGT TCA GTT GAT GAA GCT CTC CCT TCA TTT TTA GGA ATC TAT AAT GGT AAA CTC TCA GAG
CCT AAT CTT AAA GAA TTC GTG GAA TCA GCC GAC TTC ATC CTG ATG CTT GGA GTT AAA CTC ACA GAC
TCT TCA ACA GGA GCC TTC ACT CAT CAT TTA AAT GAA AAT AAA ATG ATT TCA CTG AAT ATA GAT GAA
GGA AAA ATA TTT AAC GAA AGC ATC CAA AAT TTT GAT TTT GAA TCC CTC ATC TCC TCT CTC TTA GAC
CTA AGC GAA ATA GAA TAC AAA GGA AAA TAT ATC GAT AAA AAG CAA GAA GAC TTT GTT CCA TCA AAT
GCG CTT TTA TCA CAA GAC CGC CTA TGG CAA GCA GTT GAA AAC CTA ACT CAA AGC AAT GAA ACA ATC
GTT GCT GAA CAA GGG ACA TCA TTC TTT GGC GCT TCA TCA ATT TTC TTA AAA CCA AAG AGT CAT TTT
ATT GGT CAA CCC TTA TGG GGA TCA ATT GGA TAT ACA TTC CCA GCA GCA TTA GGA AGC CAA ATT GCA
GAT AAA GAA AGC AGA CAC CTT TTA TTT ATT GGT GAT GGT TCA CTT CAA CTT ACG GTG CAA GAA TTA

GGA TTA GCA ATC AGA GAA AAA ATT AAT CCA ATT TGC TTT ATT ATC AAT AAT GAT GGT TAT ACA GTC
GAA AGA GAA ATT CAT GGA CCA AAT CAA AGC TAC AAT GAT ATT CCA ATG TGG AAT TAC TCA AAA TTA
CCA GAA TCA TTT GGA GCA ACA GAA GAA CGA GTA GTC TCG AAA ATC GTT AGA ACT GAA AAT GAA TTT
GTG TCT GTC ATG AAA GAA GCT CAA GCA GAT CCA AAT AGA ATG TAC TGG ATT GAG TTA ATT TTG GCA
AAA GAA GAT GCA CCA AAA GTA CTG AAA AAA ATG GGC AAA CTA TTT GCT GAA CAA AAT AAA TCA GGA
TCC CTG GTG CCG CGC GGC AGC TGT CGC AGC AAT GCC GTA GCA GAA CAG GGC CGC AAG ACT CAG GAG
TTT ACC CAG CAA TCA GCG CAA TAC GTC GAA GCT GCC CGC AAA CAC TAT GAC GCG GCG GAA AAG CTC
AAC ATC CCT GAC TAT CAG GAG AAA GAA GAC GCA TTT ATG CAA CTG GTT CCG CCT GCG GTT GGG GCC
GAC ATT ATG CGC CTG TTC CCG GAA AAG TCC GCC GCG CTC ATG TAT CAC CTG GGG GCA AAC CCG GAG
AAA GCC CGC CAG TTA CTG GCG ATG GAT GGG CAG TCC GCG CTG ATT GAA CTC ACT CGA CTA TCC GAA
CGC TTA ACT CTC AAG CCT CGC GGT AAA CAA ATC TCT TCC GCT CCC CAT GCT GAC CAG CCT ATT ACC
GGT GAT GTC AGC GCA GCA AAT AAA GAT GCC ATT CGT AAA CAA ATG GAT GCT GCT GCG AGC AAG GGA
GAT GTG GAA ACC TAC CGC AAG CTA AAG GCA AAA CTT AAA GGA ATC CGA TAA

AdhA-SP$_{141}$

ATG GCG AAA GCA GCA GTA GTA AGA CAC AAT CCA GAT GGT TAT GCG GAC CTT GTT GAA AAG GAA CTT
CGA GCA ATC AAA CCT AAT GAA GCT TTG CTT GAC ATG GAG TAT TGT GGA GTC TGT CAT ACC GAT TTG
CAC GTT GCA GCA GGT GAT TAT GGC AAC AAA GCA GGG ACT GTT CTT GGT CAT GAA GGA ATT GGA ATT
GTC AAA GAA ATT GGA GCT GAT GTA AGC TCG CTT CAA GTT GGT GAT CGG GTT TCA GTG GCT TGG TTC
TTT GAA GGA TGT GGT CAC TGT GAA TAC TGT GTA TCT GGT AAT GAA ACT TTT TGT CGA GAA GTT AAA
AAT GCA GGA TAT TCA GTT GAT GGC GGA ATG GCT GAA GAA GCA ATT GTT GTT GCC GAT TAT GCT GTC
AAA GTT CCT GAC GGA CTT GAC CCA ATT GAA GCT AGC TCA ATT ACT TGT GCT GGA GTA ACA ACT TAC
AAA GCA ATC AAA GTA TCA GGA GTA AAA CCT GGT GAT TGG CAA GTA ATT TTT GGT GCT GGA GGA CTT
GGA AAT TTA GCA ATT CAA TAT GCT AAA AAT GTT TTT GGA GCA AAA GTA ATT GCT GTT GAT ATT AAT
CAA GAT AAA TTA AAT TTA GCT AAA AAA ATT GGA GCT GAT GTG ATT ATC AAT TCT GGT GAT GTA AAT
CCA GTT GAT GAA ATT AAA AAA ATA ACT GGC GGC TTA GGG GTG CAA AGT GCA ATA GTT TGT GCT GTT
GCA AGG ATT GCT TTT GAA CAA GCG GTT GCT TCT TTG AAA CCT ATG GGC AAA ATG GTT GCT GTG GCA
CTT CCC AAT ACT GAG ATG ACT TTA TCA GTT CCA ACA GTT GTT TTT GAC GGA GTG AGG TTG CAG TTC
ACT TGT CGG ACA GAC TTG ACT TGG CAG AGC TTT TCA ATT TGG AGC AGA CGT AGT AAA CCA ATT GTT
GCG ACA CGC AAA CTG GAA GAA ATC AAT GAT ATT ATT GAT GAA ATG AAG GCA GGA AAA ATT GAA GGC
CGA ATG GTC ATT GAT TTT ACT AAA GGA TCC CTG GTG CCG CGC GGC AGC TGT CGC AGC AAT GCC GTA
GCA GAA CAG GGC CGC AAG ACT CAG GAG TTT ACC CAG CAA TCA GCG CAA TAC GTC GAA GCT GCC CGC
AAA CAC TAT GAC GCG GCG GAA AAG CTC AAC ATC CCT GAC TAT CAG GAG AAA GAA GAC GCA TTT ATG
CAA CTG GTT CCG CCT GCG GTT GGG GCC GAC ATT ATG CGC CTG TTC CCG GAA AAG TCC GCC GCG CTC
ATG TAT CAC CTG GGG GCA AAC CCG GAG AAA GCC CGC CAG TTA CTG GCG ATG GAT GGG CAG TCC GCG
CTG ATT GAA CTC ACT CGA CTA TCC GAA CGC TTA ACT CTC AAG CCT CGC GGT AAA CAA ATC TCT TCC
GCT CCC CAT GCT GAC CAG CCT ATT ACC GGT GAT GTC AGC GCA GCA AAT AAA GAT GCC ATT CGT AAA
CAA ATG GAT GCT GCT GCG AGC AAG GGA GAT GTG GAA ACC TAC CGC AAG CTA AAG GCA AAA CTT AAA
GGA ATC CGA TAA

Section 2. Supplementary Tables in the Methods section

Supplementary Table S1. Amino acid sequences of P22 CP and engineered P22 CP mutant, which have extra peptide located at the C-terminus. Two repeats of E peptide is underlined.

Proteins	Amino Acid Sequence
CP without E2 (wtCP)	MALNEGQIVTLAVDEIIETISAITPMAQKAKKYTPPAACMQRSSNTIWMPVEQESPTQEGWDLTDKATG LLELNVAVNMGEPDNDFFQLRADDLRDETAYRRRIQSAARKLANNVELKVANMAAEMGSLVITSPDAIG TNTADAWNFVADAEEIMFSRELNRDMGTSYFFNPQDYKKAGYDLTKRDIFGRIPEEAYRDGTIQRQVAG FDDVLRSPKLPVLTKSTATGITVSGAQSFKPVAWQLDNDGNKVNVDNRFATVTLSATTGMKRGDKISFA GVKFLGQMAKNVLAQDATFSVVRVVDGTHVEITPKPVALDDVSLSPEQRAYANVNTSLADAMAVNILNV KDARTNVFWADDAIRIVSQPIPANHELFAGMKTTSFSIPDVGLNGIFATQGDISTLSGLCRIALWYGVN ATRPEAIGVGLPGQTA
CP with E2 (CP-E2)	MALNEGQIVTLAVDEIIETISAITPMAQKAKKYTPPAASMQRSSNTIWMPVEQESPTQEGWDLTDKATG LLELNVAVNMGEPDNDFFQLRADDLRDETAYRRRIQSAARKLANNVELKVANMAAEMGSLVITSPDAIG TNTADAWNFVADAEEIMFSRELNRDMGTSYFFNPQDYKKAGYDLTKRDIFGRIPEEAYRDGTIQRQVAG FDDVLRSPKLPVLTKSTATGITVSGAQSFKPVAWQLDNDGNKVNVDNRFATVTLSATTGMKRGDKISFA GVKFLGQMAKNVLAQDATFSVVRVVDGTHVEITPKPVALDDVSLSPEQRAYANVNTSLADAMAVNILNV KDARTNVFWADDAIRIVSQPIPANHELFAGMKTTSFSIPDVGLNGIFATQGDISTLSGLCRIALWYGVN ATRPEAIGVGLPGQTATSVAALQSQVAALQSQ*

Supplementary Table S2. Primer sequences used to clone KivD and AdhA from *L. lactis* genomic DNA.

	Forward Primer	Reverse Primer
KivD	AAAGACATATGCCATGGCATATACAGTAGGAG ATTACCTATTAG	AGAAGACTCGAGGGATCCTGATTTATTTTGTT CAGCAAATAG
AdhA	ATATCCATGGCGAAAGCAGCAGTAGTAAGACA CAATCCAGATGG	ATATGGATCCTTTAGTAAAATCAATGACCATT CGGCCTTCAATTTTTCCTG

Section 3. Characterization of P22 VLPs

Morphologies of various P22 VLPs prepared in this study were observed by TEM (Supplementary Figure S1). Cage-like morphology of wtP22 and P22-E2 were indistinguishable, indicating that genetic fusion of the E2 peptide (*i.e.* $(VAALEKE)_2$) at the C-terminus of the CP did not alter overall capsid structure of P22 VLP. Hydrodynamic diameters (D_h) of the VLPs were analyzed with DLS (Supplementary Figure S2). D_h of the P22-E2 was about 2 nm larger than that of wtP22. It has been revealed that the C-terminus of the CP is exposed to the exterior of the capsid[1]. Because up to 420 copies of E2, peptide would be presented on the exterior surface of the P22-E2 VLPs, it is reasonable that P22-E2 VLP have slightly larger D_h than wtP22 VLP. Zeta-potentials of the VLPs were determined by electrophoretic mobility measurements (Figure 2b). The P22-E2 showed a negative surface charge almost identical to wtP22 suggesting that the negatively charged E2 peptide does not alter the overall surface charge of the VLP.

To investigate assembly of P22 VLPs into a bulk material mediated by dendrimers, we first mixed wtP22 with either an amine-terminated generation 6 PAMAM dendrimer (G6, positively charged) or a carboxyl-terminated generation 6.5 dendrimer (G6.5, negatively charged) in buffer solutions (pH 7.0) with a range of ionic strengths (I). Assembly of VLPs was evaluated by the turbidity of sample solutions monitored with UV-Vis spectroscopy. The wtP22 VLP assembled to large aggregates upon addition of positively charged G6 (1000 G6 per VLP) at ionic strengths up to I = 247 mM, whereas the VLP did not assemble upon addition of negatively charged G6.5 over the entire range of ionic strengths tested (Supplementary Figure S3). This result indicates that the assembly is mediated through electrostatic interactions between negatively charged P22 VLP and positively charged G6 dendrimer.

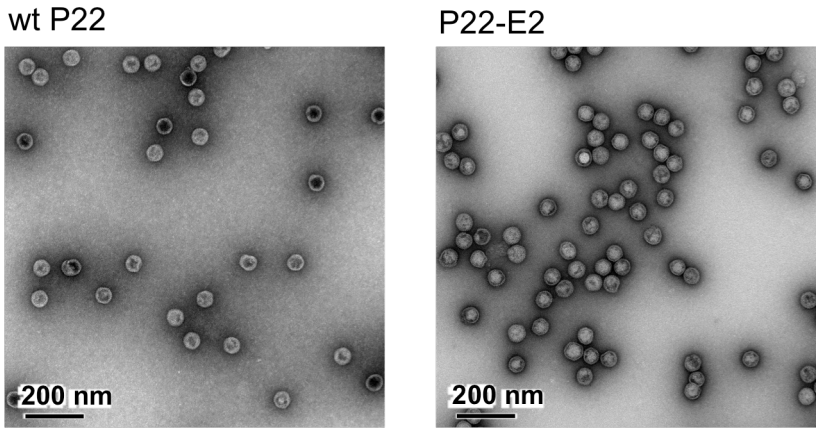

Supplementary Figure S1. TEM images of wtP22 and P22-E2 VLPs. Both the VLP constructs assembled to capsid structures with diameters of about 55 nm regardless of the modification to the coat proteins. The samples were stained with 2% uranyl acetate.

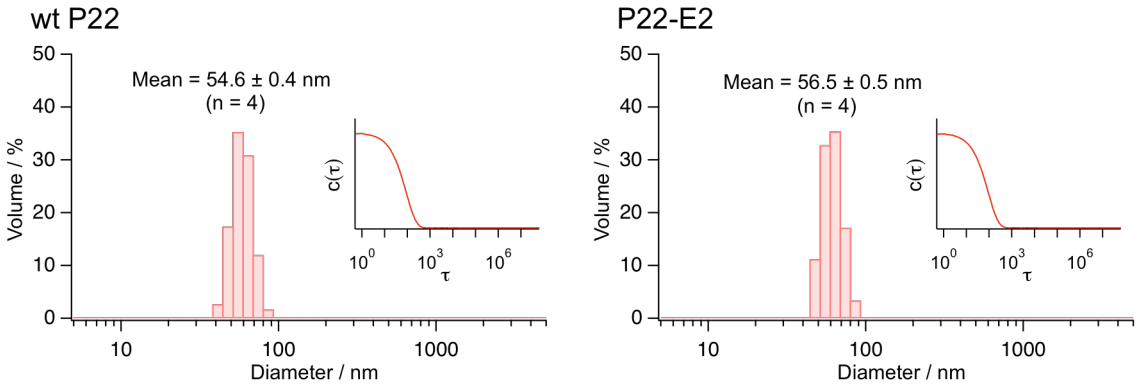

Supplementary Figure S2. Volume-averaged hydrodynamic diameter of wtP22 and P22-E2 VLPs measured with DLS and corresponding correlation functions (inset). The hydrodynamic diameter of P22-E2 was slightly larger than that of wtP22 likely due to 420 copies of E2 peptide exposed on the exterior surface of the VLP.

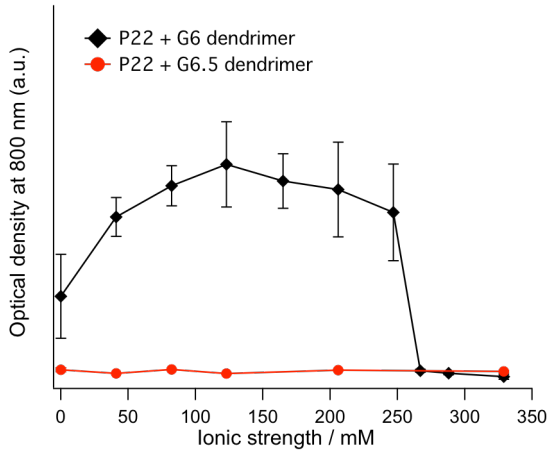

Supplementary Figure S3. Assembly of wtP22 VLPs with PAMAM dendrimers. Assembly of wtP22 mediated by either positively charged G6 PAMAM dendrimers or negatively charged G6.5 dendrimers was assessed in solutions with varying ionic strength (*I*) using light scattering at 800 nm. An increase in optical density due to formation of large aggregates was observed upon addition of G6 under *I* = 0 – 247 mM, whereas no increase was observed upon addition of G6.5 through the entire range of ionic strength tested.

Section 4. Ionic strengths and Debye screening lengths of buffer solutions used in this study

Higher order assembly of wtP22 VLP and P22-E2 variant, mediated by G6 dendrimer were investigated in solutions with a range of ionic strengths (I) to modulate the magnitude of the electrostatic interactions (Supplementary Table S3). Each type of P22 VLP assembled into larger aggregates up to a certain ionic strength (Figure 2). We define the ionic strength above which assembly does not occur as the threshold ionic strength (I_T). A critical factor that contributes to the ionic strength threshold is charge screening, described by the Debye screening length κ^{-1}, the distance over which electrostatic interactions between particles become attenuated in solution.

$$\kappa^{-1} = \sqrt{\frac{\varepsilon_0 \varepsilon_r k_B T}{2 N_A e^2 I}}$$

(where ε_0 is vacuum permittivity, ε_r is relative permittivity of the solvent, k_B is the Boltzmann constant, T is absolute temperature, N_A is Avogadro's number, e is the elementary charge, and I is ionic strength). Under the ionic strengths tested, the Debye screening lengths (κ^{-1}) are in the range of 0.5 nm (I = 329 mM) to 1.5 nm (I = 41.1 mM) (Supplementary Table S3), which is much smaller than the size of P22 VLPs (56 nm diameter) and G6 (6.7 nm diameter). With increasing ionic strength, surface charges of P22 and G6 are effectively screened and the Debye length becomes shorter. Thus, above the I_T, the short-range attractive interactions become too weak to overcome steric hindrance or thermal energy, and assembly does not occur.

Supplementary Table S3. Ionic strength, salt concentrations and calculated Debye length of buffer solutions used in this study. All the buffers are adjusted to pH 7.0

Ionic strength / mM	Sodium Phosphate / mM	Sodium Chloride / mM	Debye length / nm
0	0	0	-
41.1	10	20	1.5
61.7	15	30	1.2
82.3	20	40	1.1
123	30	60	0.87
165	40	80	0.75
206	50	100	0.67
247	60	120	0.61
288	70	140	0.57
329	80	160	0.53

Section 5. Modeling of scattering data obtained from P22 + G6 assemblies

SAXS data obtained from samples of P22 arrays mediated with G6 consist of two types of x-ray scattering: form factor *P(q)*, which is inherent to the sizes and shapes of individual nanoparticles, and scattering factor *S(q)*, which is inherent to the arrangement of these nanoparticles relative to one another. The overall x-ray scattering intensity *I(q)*, which is measured experimentally, is a combination of these two types of scattering and given as follows[2];

$$I(q) = kP(q)S(q)$$

where the constant k is a factor related to the concentration of particles, and q is the modulus of scattering vector **q**. Because the arrangement of P22 VLPs is the primary interest of this work, *S(q)* is the most relevant data for structure determination. *S(q)* curves presented in Figures 3a and 3b in the main text and Supplementary Figure S19 in the Supporting Information Section 13 are generally obtained by dividing measured *I(q)* by modeled *kP(q)*. When the particles form crystalline assemblies in this work, they generate diffuse scattering due to the defect of the second kind[3-5], which affects the intensities at the minima position of *P(q)*[6-7]. This indicates that the scattering due to the structural defects affects the form factor scattering and dividing *I(q)* by the experimentally obtained *P(q)* from P22 VLPs used in this study would produce artificial peaks in *S(q)* at the minima of *P(q)*. To prevent this from happening we modeled the diffuse scattering with a power-law function (c/q^n, where c and n are constants) and fit *I(q)* with sum of the experimental *P(q)*, $P_e(q)$, and the power function as:

$$I(q) = k(P_e(q) + c/q^n)S(q)$$

S(q) is then obtained by dividing *I(q)* by *P(q)*, which is $P_e(q) + c/q^n$. Measured *I(q)* data of each sample is presented in Supplementary Figure S4 and the comparison between measured *I(q)*, modeled *kP(q)* and extracted *S(q)* are presented in Supplementary Figure S5.

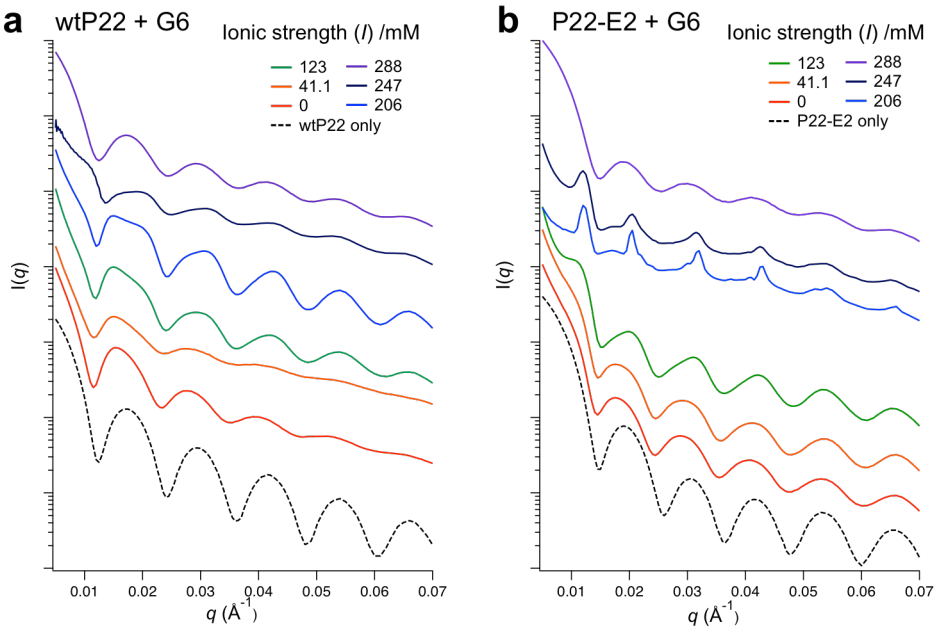

Supplementary Figure S4. Measured SAXS patterns (I(*q*) *versus* q) of **(a)** wtP22 and **(b)** P22-E2 with G6 dendrimer under various ionic strengths. Plots are vertically offset for clarity.

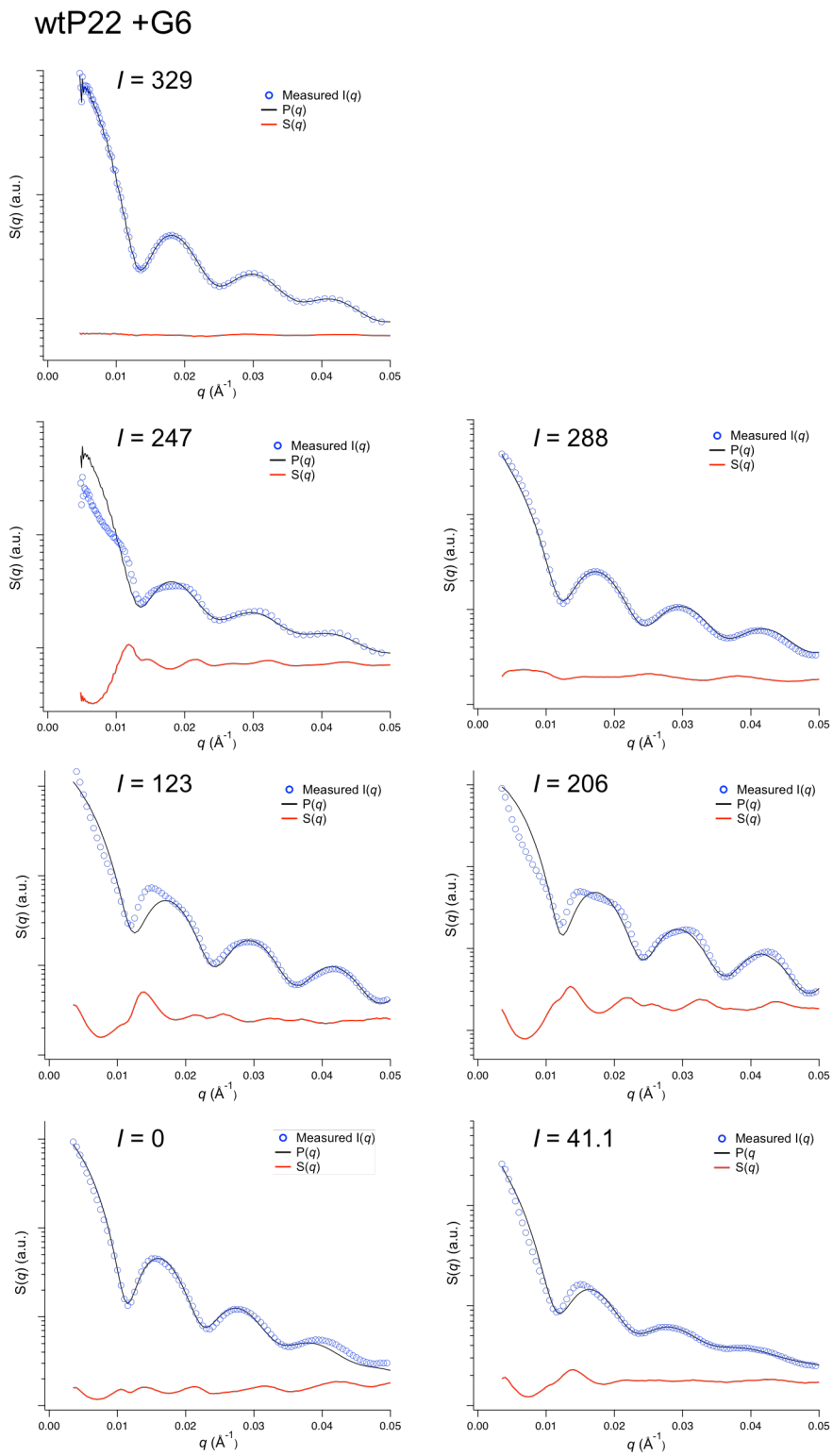

Supplementary Figure S5. Plots of measured *I(q)*, modeled *P(q)* and extracted *S(q)* SAXS data. In all plots, the blue trace is experimentally obtained *I(q)* of each sample, and the black trace is the modeled form factor *P(q)*. The structure factor *S(q)* (red trace) was obtained by dividing *I(q)* by *P(q)*. The *S(q)* plots are vertically offset for clarity.

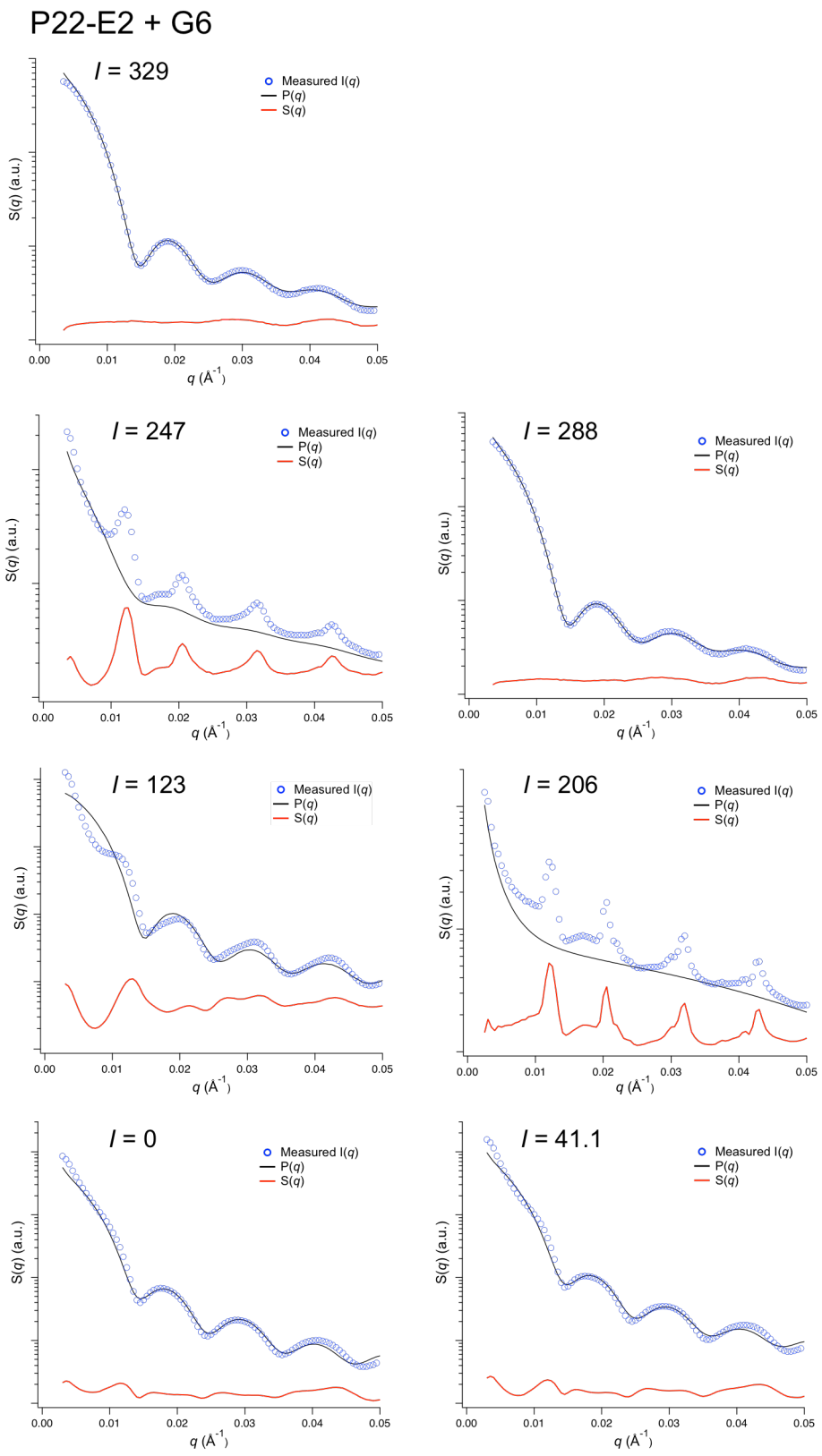

Supplementary Figure S5. (continued)

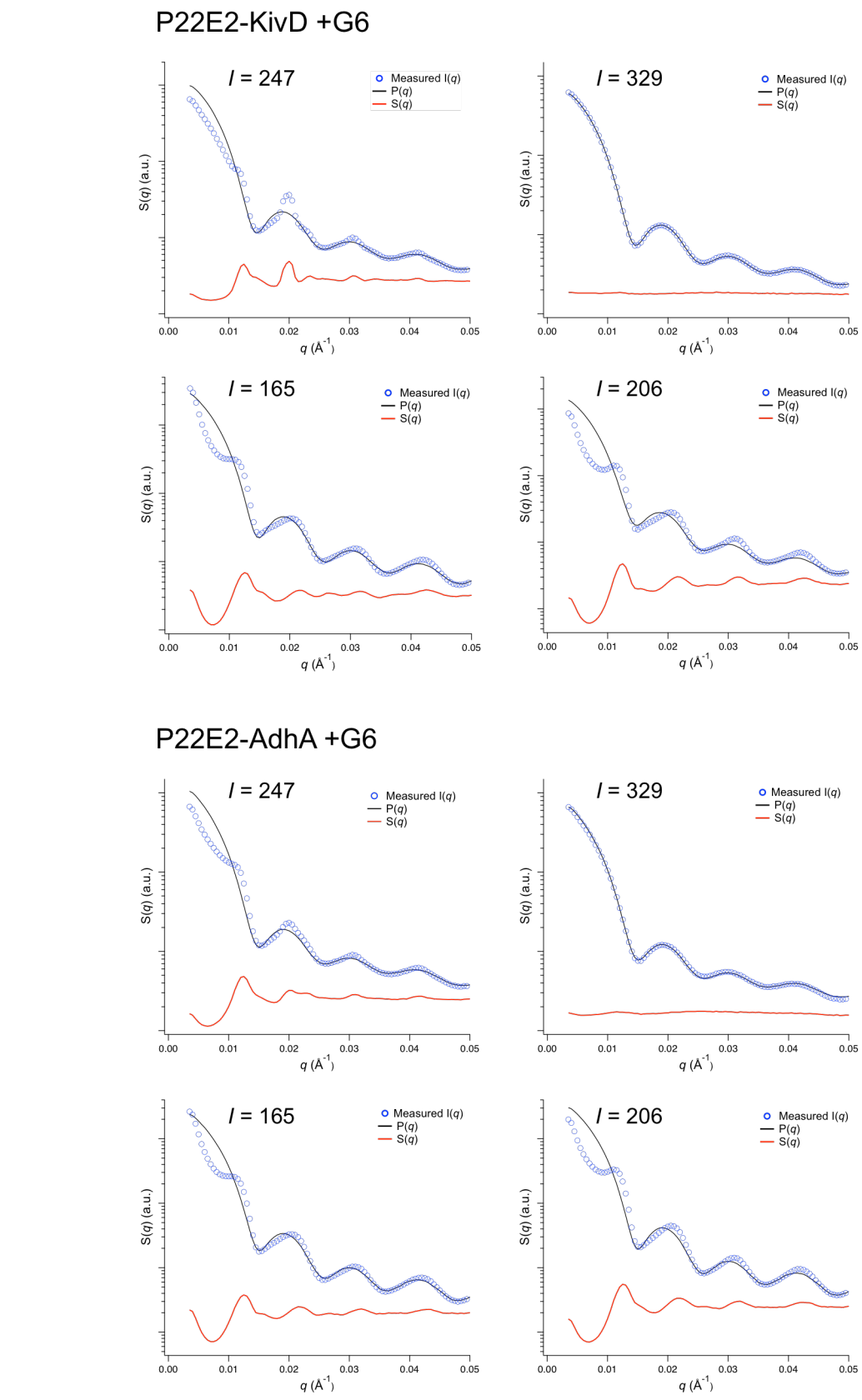

Supplementary Figure S5. (continued)

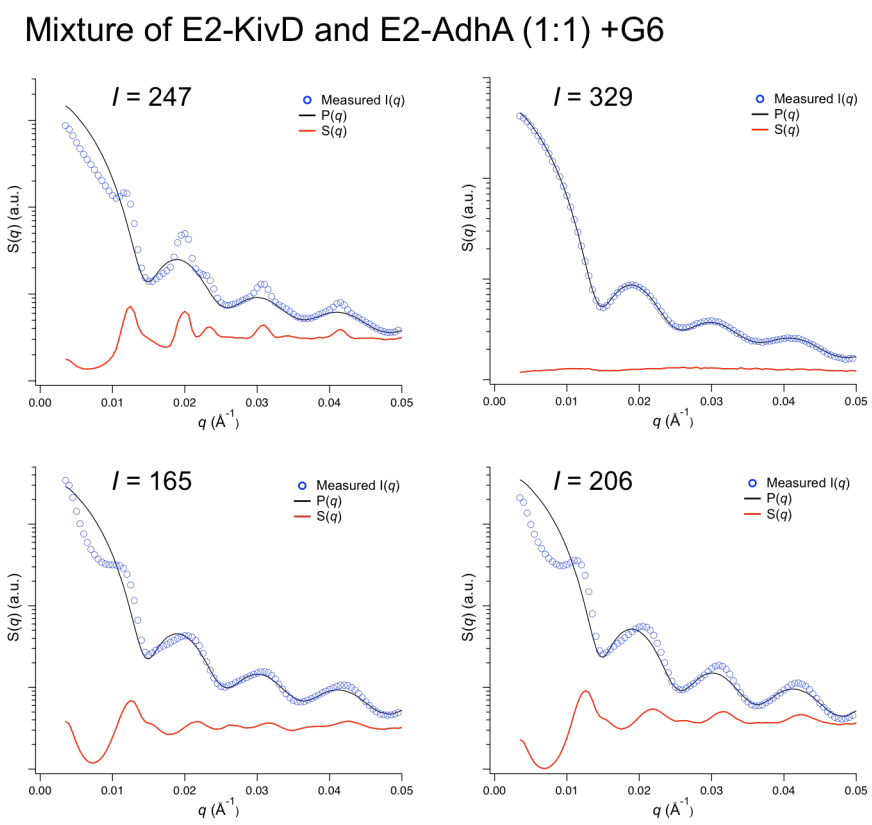

Supplementary Figure S5. (continued)

Section 6. Additional SAXS data and analysis of superlattices composed of P22-E2 and G6

The form factor scattering of P22-E2 in solution was analyzed for simulating the SAXS of assemblies accurately. The pair distance distribution function $P(r)$ was obtained by fitting the experimental form factor scattering $P(q)$ of P22-E2 in solution using the maximum entropy method (Supplementary Figure S6). The calculated $P(r)$ shows a peak at a distance r that is closer to the radius of P22-E2 than its diameter, indicating that the P22-E2 is not an empty capsid and filled with something, which are scaffolding proteins in this case.

Supplementary Figure S7 compares our solution model *versus* the PDB model (PDB ID: 2XYY). In the PDB model, P22 is an empty capsid in a vacuum. The solution model is generated by positioning water molecules into the PDB model with a mean electron density of 0.3344 electrons/Å^3. In addition to this, the empty inner space of P22-E2 is filled with scaffolding

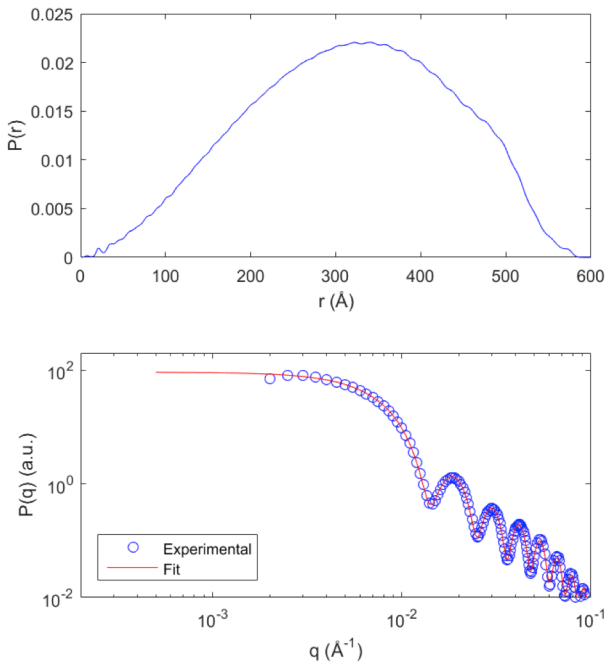

Supplementary Figure S6. Pair distance function $P(r)$ (top) and form factor scattering $P(q)$ (bottom) of P22-E2.

proteins, leading to non-zero electron density difference (Δρ) inside the capsid (Supplementary Figure S7a). The $P(r)$s of the two models, with and without scaffolding proteins, are clearly different from each other as shown in Supplementary Figure S7b. The $P(r)$ of the PDB model is indeed a characteristic $P(r)$ of a core-shell structure[8]. On the other hand, the $P(r)$ of our solution model is similar to the experimentally determined one shown in Supplementary Figure S6. These different morphologies result in notable difference in $P(q)$ (Supplementary Figure S7c) and thereby $I(q)$ (Supplementary Figure S7d). The calculated $I(q)$ from the PDB model could not accurately describe intensities of (111) and (200) reflections as shown in Supplementary Figure S7d.

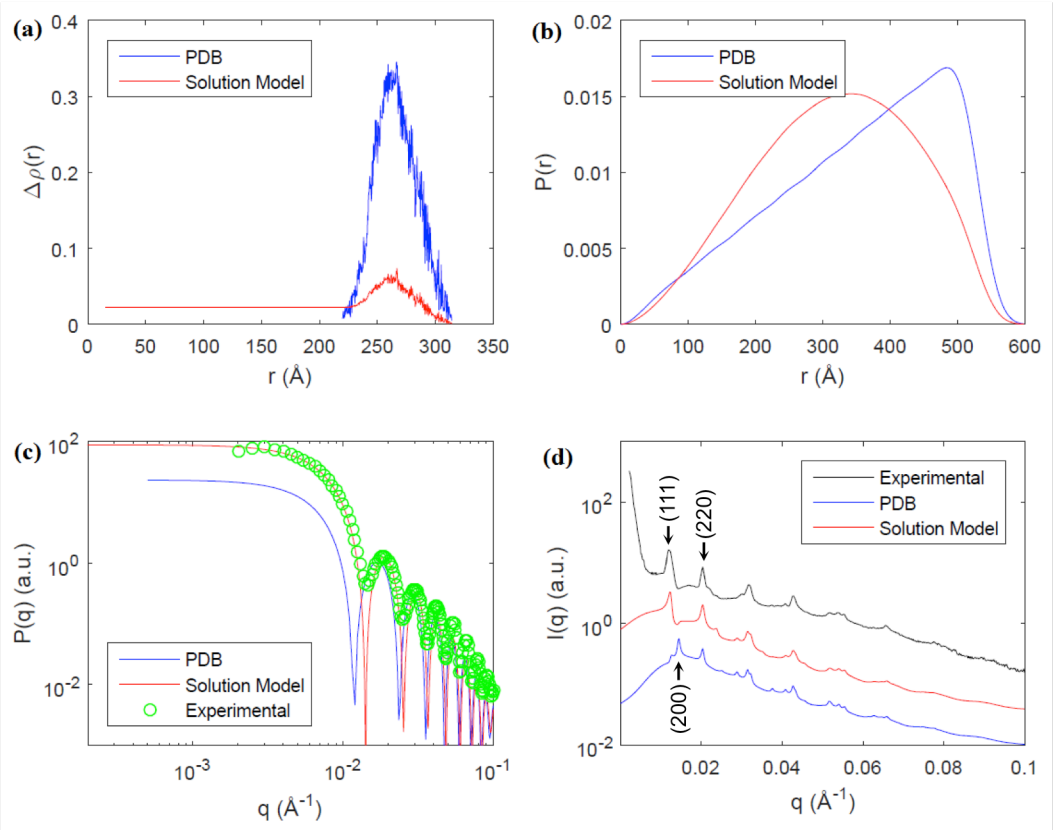

Supplementary Figure S7. Plots of **(a)** electron density differences $(\Delta\rho)$ and **(b)** pair distance distribution function $P(r)$ of the PDB model (PDB ID: 2XYY) and solution models. **(c)** $P(q)$s calculated using the two models are compared with the experimental $P(q)$ of P22-E2. **(d)** $I(q)$s calculated using *P(q)*s of the two models are compared with the experimental $I(q)$ obtained from the superlattice of P22-E2 and G6 prepared at ionic strength of 206 mM.

We have measured several samples of P22-E2 and G6 superlattice prepared under the same ionic strength condition (I = 206 mM). All the samples showed predominant peaks that were attributed to an FCC structure. In some samples, minor peaks (q = 0.0175, 0.0221, 0.0302) that were assigned to an HCP structure were detected. Supplementary Figure S8 compares the experimental $I(q)$ of a sample (black profile), showing the most intense HCP peaks among all of the measured samples, with simulated peaks of FCC (a = 87 nm; blue profile) and HCP (a = 61.5 nm, c = 101.1 nm; green profile) lattice models. Linear superposition of 70% FCC and 30% HCP (red profile) results in a good agreement with the experimental data, suggesting that FCC is dominant over HCP.

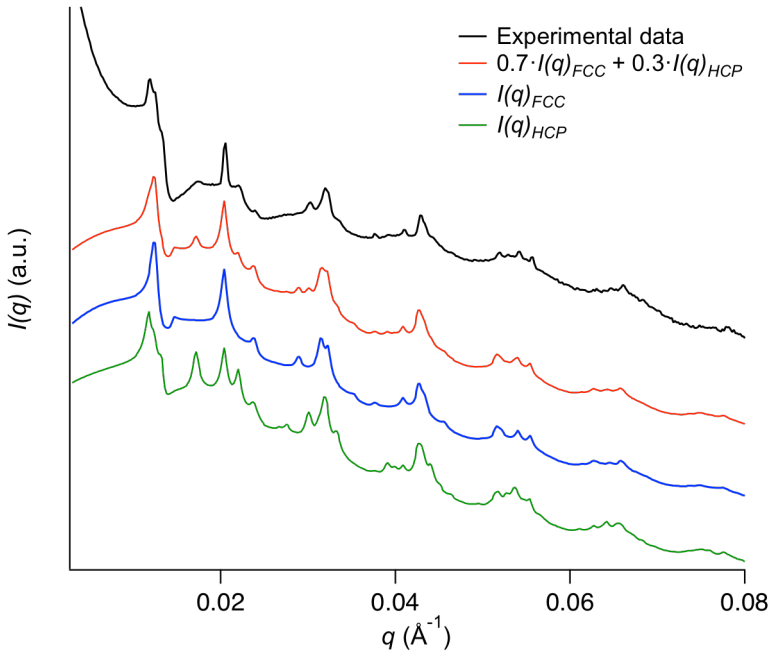

Supplementary Figure S8. Comparison of experimental $I(q)$ and simulated plots of FCC and HCP models. The lattice constant for FCC is 87.0 nm. HCP lattice constants are a = 61.5 and c = 101.1 nm. Data are scaled arbitrarily for visual clarity.

Section 7. Estimation of crystalline domain size from SAXS

Crystalline domain size is inversely proportional to the x-ray diffraction peak width[2], enabling the domain size estimation from SAXS data. We analyzed peak widths of first order reflections to minimize potential artefacts due to micro-strain[2]. We note that the domain size denotes a mass averaged size of single crystalline domains if the assemblies are polycrystalline[2]. Peak width is a convenient parameter to compare samples prepared under different conditions and to monitor crystallization behavior. Here, Gaussian functions were used to fit the first order diffraction peaks and to determine the full width at half maximum (FWHM) (Supplementary Table S4). Instrumental resolution Δq_{inst}, which leads to peak broadening, was taken into account and the resolution-corrected FWHM of a sample peak, Δq_{samp}, is given by the following form for a convolution of two Gaussians:

$$\Delta q_{samp} = \sqrt{\Delta q_{obs}^2 - \Delta q_{inst}^2}$$

where Δq_{obs} is the FWHM of an observed diffraction peak, and Δq_{inst} for our measurement is approximately 0.0005 $Å^{-1}$.

Crystalline domain size *d* (Supplementary Table S4) was calculated using the Scherrer equation:

$$d = \frac{K\lambda}{\beta cos\theta}$$

where K is the Scherrer's constant, λ is the x-ray wavelength used for the measurements (0.8856 Å), β is the resolution-corrected peak width in radians, and θ is half of the scattering angle 2θ. Although the value of K depends on factors such as geometry of the crystallites, 0.9

may be taken for roughly equant crystallites when the FWHM is used as the measure of peak width[9-10].

Supplementary Table S4. The full width at half maximum (FWHM) of observed first order diffraction peak, the resolution-corrected FWHM, and estimated domain size of each sample.

wtP22 + G6

I / mM	Δq_{obs} / Å	Δq_{samp} / Å	Estimated domain size / nm
0	0.00364	0.00360	156.9
41.1	0.00357	0.00353	160.2
123	0.00309	0.00305	185.4
206	0.00307	0.00303	186.8
247	0.00303	0.00299	189.4
288	No Assembly	-	-
329	No Assembly	-	-

P22-E2 + G6

I / mM	Δq_{obs} / Å	Δq_{samp} / Å	Estimated domain size / nm
0	0.00372	0.00369	153.3
41.1	0.00344	0.00340	166.2
123	0.00308	0.00303	186.3
206	0.00148	0.00139	406.6
247	0.00203	0.00197	287.6
288	No Assembly	-	-
329	No Assembly	-	-

Section 8. Optical microscopy and TEM analysis of superlattices composed of P22-E2 and G6

Assembled samples of P22-E2 and G6, prepared at I = 206 mM (sodium phosphate 50 mM, sodium chloride 100 mM, pH7.0), were investigated by optical microscopy (Axio; Carl Zeiss AG, Oberkochen, Germany) and transmission electron microscopy (TEM). Suspensions of the VLP assembly in buffer were observed by optical microscopy with differential interference contrast (DIC) and exhibited discrete particles 1 – 10 μm in size (Supplementary Figure S9).

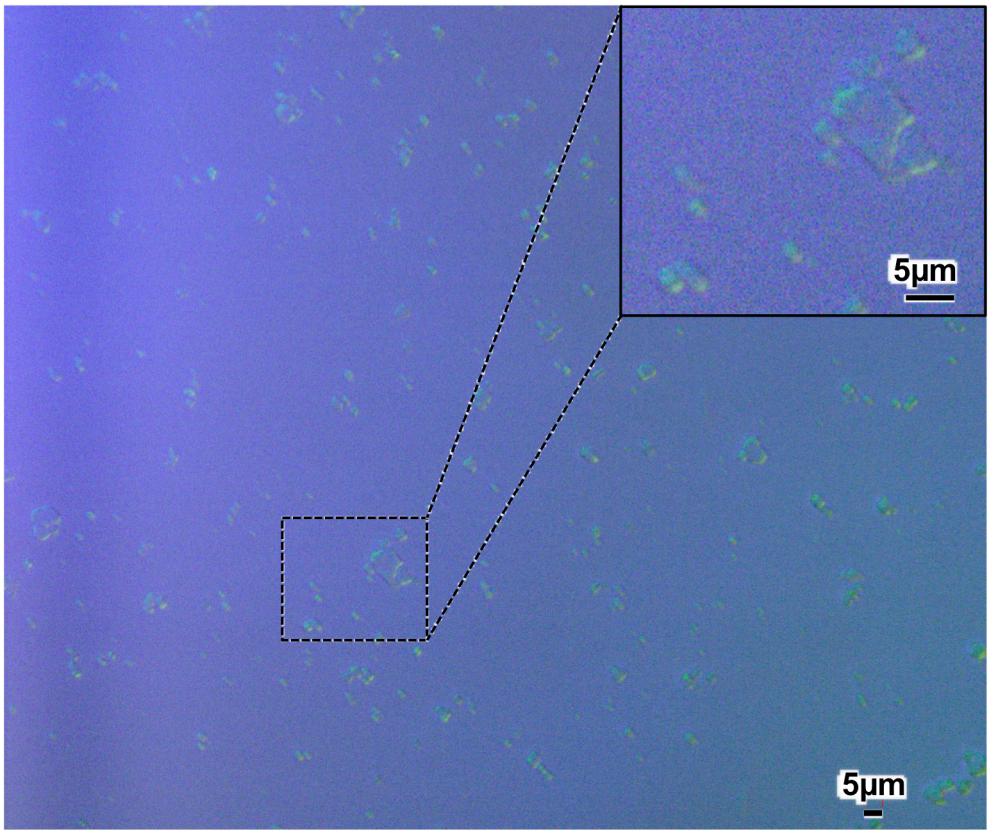

Supplementary Figure S9. DIC image of P22-E2 assembly mediated by G6 in buffer of I = 206 mM. Inset is a magnified version of the selected region. Discrete particles in 1 – 10 μm size range were observed in the solution sample.

TEM observation revealed that the assembled particles have a highly ordered structure, which is consistent with an FCC lattice of P22 particles (Figure 4a and Supplementary Figure S10). Assembled samples were shadowed with Pt-Pd before TEM imaging. Because the Pt-Pd is deposited on the top of the samples, the method enhances the contrast of the surface roughness and fine structure, allowing us to observe surface morphology of the samples even if they are relatively thick with multi layers of VLPs. In an FCC structure, each particle adopts a hexagonal close packed arrangement on the {111} lattice planes, and square packed arrangement on {100} lattice planes. The assembled samples showed hexagonal close packing with an inter-row spacing of about 54 nm in most areas where the assembled bulk was thin enough to observe (Figure 4a1). The inter-row spacing of 54 nm for the hexagonal lattice corresponds to a nearest neighbor distance of 62 nm between the VLPs, consistent with the {111} lattice plane of an FCC structure with a = 87 nm. A square packed arrangement of VLPs was also observed in some assemblies (Figure 4a2) and the observed center-to-center distance between the nearest neighbor VLPs of about 61 nm is in good agreement with the {100} lattice planes of an FCC structure with a = 87 nm.

A sample for conventional TEM needs to be dried, hence there is a concern regarding artefact formation due to the drying process. In order to further confirm the structure of the P22-E2 array in the absence of any drying effects, the assembly of P22-E2 and G6 dendrimer was investigated by cryo-EM. Hexagonal close packing with an inter-row spacing of about 55 nm was observed (Supplementary Figure S11). This corresponds to a 63 nm particle-to-particle distance, almost the same as that observed in the dried sample with conventional TEM (Figure 4a and Supplementary Figure S10). Together with the results from the SAXS measurements, this suggests that the hexagonal closed packing of VLPs observed by both techniques is not due to drying artefacts but rather represents the true structure of the assembly.

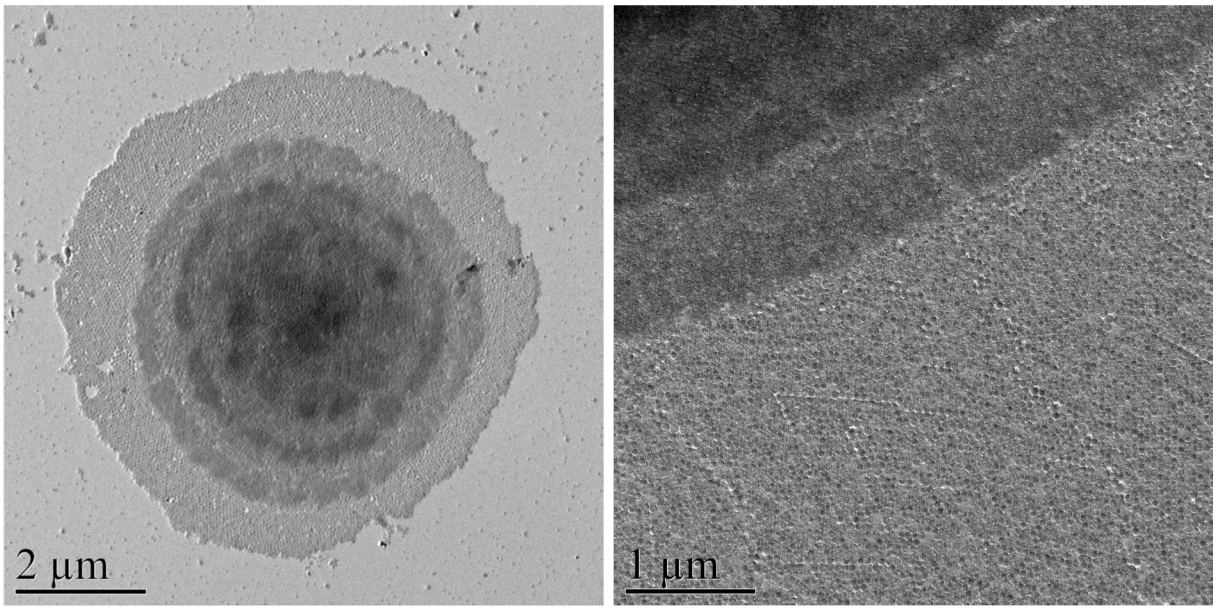

Supplementary Figure S10. Additional TEM images of P22-E2 assembly mediated by G6 at ionic strength of 206 mM. The assembled samples were shadowed with Pt-Pd prior to TEM observation.

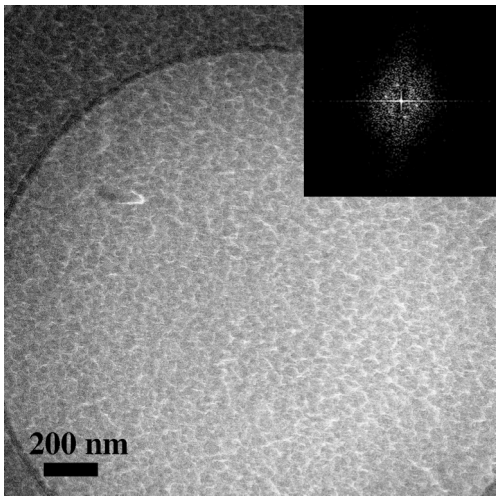

Supplementary Figure S11. Cryo-EM of P22-E2 assembly mediated by G6 at ionic strength of 206 mM. FFT image indicates that closed packed arrays with the inter-row spacing of 55 nm were formed. The inter-row spacing distance corresponds to a nearest particle-particle distance of 63 nm.

Section 9. Quantification of G6 / P22-E2 ratio in the ordered superlattices

The amount of G6 dendrimer incorporated into the P22-E2 superlattice prepared at I = 206 mM (sodium phosphate 50 mM, sodium chloride 100 mM, pH7.0) was assessed by two independent techniques: SAXS and amino acid analysis. The results obtained by these two approaches agreed well.

Quantification using SAXS

The array of P22-E2 and G6 formed at I = 206 mM was disassembled to individual particles in high ionic strength buffer (above the I_T) and then measured with SAXS. Because P22-E2 and G6 were dispersed in solution, the SAXS pattern obtained from the solution comprised only of the form factors of these two components. When two particles A and B are solubilized in a solution and do not interact with each other, the total scattering intensity, $I(A+B)$ of a solution containing x and y numbers of A and B particles, respectively, is given by:

$$I(A+B) = x|F(A)|^2 + y|F(B)|^2$$

$$= xP(A) + yP(B)$$

where *F(A)* and *F(B)* are the form factor amplitudes, and *P(A)* and *P(B)* are the form factor intensities arising from particles A and B, respectively.

Superlattices of P22-E2 and G6 were pelleted *via* centrifugation (21,100 g) and the supernatant was removed. The pellet was resuspended in phosphate buffer (sodium phosphate 50 mM, sodium chloride 100 mM, pH7.0) followed by an additional centrifugation to remove any residual free G6. The pellet was then resuspended in high salt buffer (sodium phosphate 80 mM, sodium chloride 160 mM, pH 7.0) to disassemble the superlattices into individual particles.

The SAXS profile of this disassembled sample was then measured and is referred to as $I(E2 + G6)$. Additionally, SAXS profiles for individual solutions of P22-E2 VLP only (50 nM) and G6 dendrimer only (37 x 10^3 nM) in the same buffer were measured (Supplementary Figure S12a) and are designated as $P(E2)$ and $P(G6)$, respectively. The SAXS profile of the E2 + G6 solution ($I(E2 + G6)$) is given as a linear combination of $P(E2)$ and $P(G6)$ with scaling factors f_{E2} and f_{G6}, as follows:

$$I(E2 + G6) = f_{E2}P(E2) + f_{G6}P(G6)$$

where the scaling factor is the ratio of the number of all particles in the mixture solution $\mathrm{E2 + G6}$ and that in the individual solutions $\mathrm{E2}$ or $\mathrm{G6}$. For example, $f_{E2} = 1$ indicates that the concentration of P22-E2 particles in the $\mathrm{E2 + G6}$ solution is identical to that of the E2 solution (*i.e.* 50 nM). Representative fitted curves are found in Supplementary Figure S12b - d. With scaling factors f_{E2} = 1.38 and f_{G6} = 0, the profiles in the low q region between 0.0025 and 0.015 Å^{-1} fit well, however peak minima and maxima in the high q region between q = 0.025 and 0.1 did not fit (Supplementary Figure S12b). By raising f_{G6} to 0.035, the calculated scattering profile fits well over a range of q = 0.0025 – 0.1 to the measured scattering of the disassembled sample (Supplementary Figure S12c). The form factors with the given scaling factors correspond to 69 nM of P22-E2 and 1295 nM of G6, therefore the G6 / P22-E2 ratio in the sample is calculated to be 18.8. The experimental errors for the ratio were determined by manually varying f_{G6} to best fit the profile. At certain f_{G6} values, best fit occurs at some portions of the profile but not others. We therefore determined the upper and lower limits of f_{G6} from the best fit to different regions of the measured profile (Supplementary Figure S12d). Accordingly the low and high limits of f_{G6} were determined to be 0.015 and 0.06, respectively, which corresponds to a G6 / P22-E2 ratio of 8.0 and 32.1.

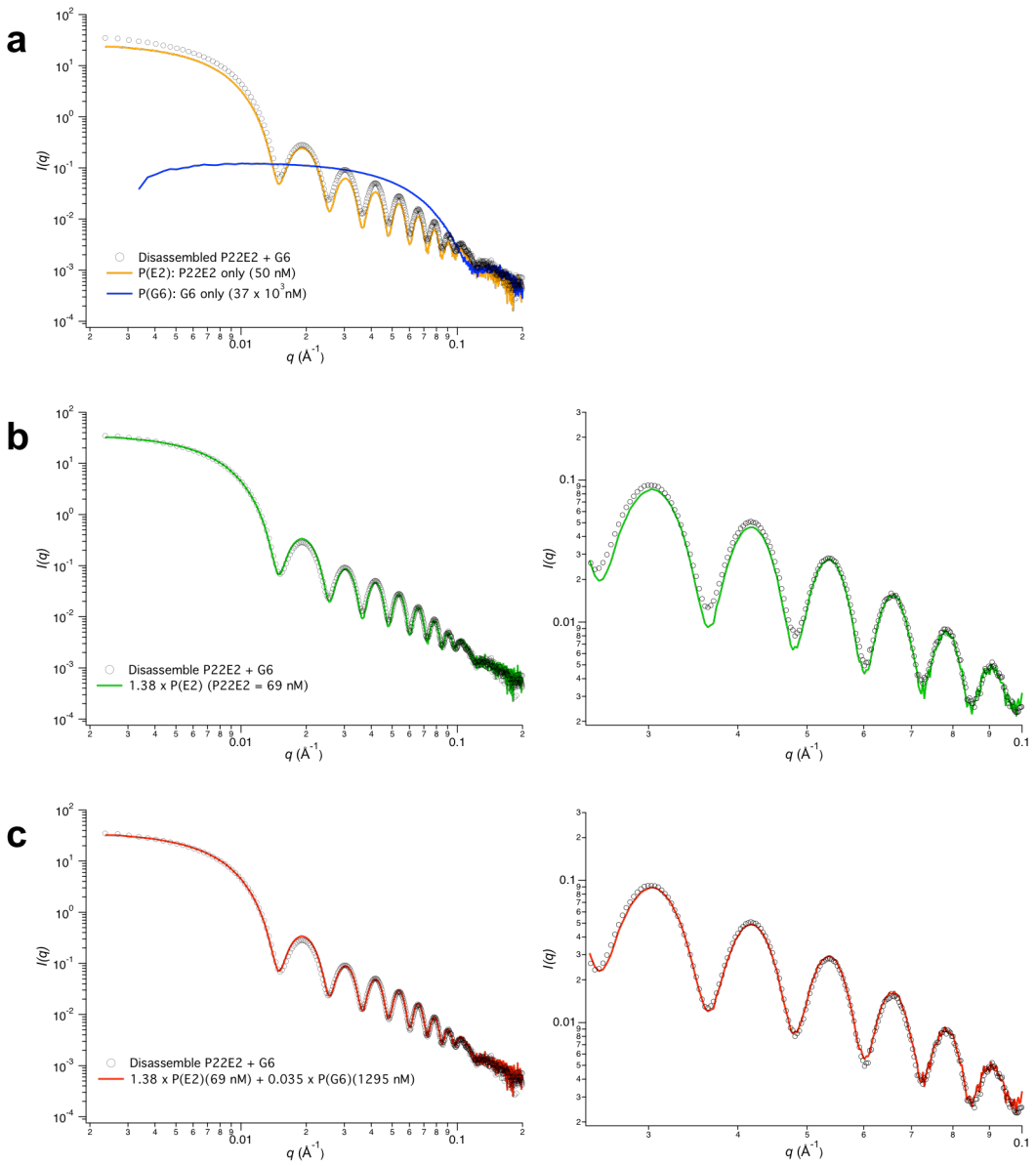

Supplementary Figure S12. Quantification of G6 dendrimers associated per P22 VLP using SAXS. a, SAXS profiles of the P22-E2 and G6 mixture disassembled from the superlattice in high salt buffer (phosphate 80mM, sodium chloride 160mM, pH 7.0) (black trace). SAXS profiles of individual P22-E2 (50 nM) (yellow) and G6 (37 x 10^3 nM) (blue) were also obtained. b, The SAXS profile of the disassembled P22-E2 + G6 sample was fit with the SAXS profile of P22-E2 alone (form factor) with a scaling factor of 1.38 (green) (left graph) and its expanded view between q = 0.025 and 0.1 (right graph). The intensity of the low q region between q = 0.0025 and 0.015 fit well, however the intensity of peak minima and maxima between q = 0.025 and 0.1 did not match. c, Calculated SAXS profile composed of the SAXS profiles of P22-E2 and G6 with scaling factors of 1.38 and 0.035, respectively (red). Not only the low q region but also intensity of peak minima and maxima between q = 0.025 and 0.1 matched well with the measured profile of the disassembled sample. The concentration of P22-E2 and G6 were determined to be 69 nM and 1295 nM, hence the G6 / P22-E2 ratio of the sample is estimated to be 18.8.

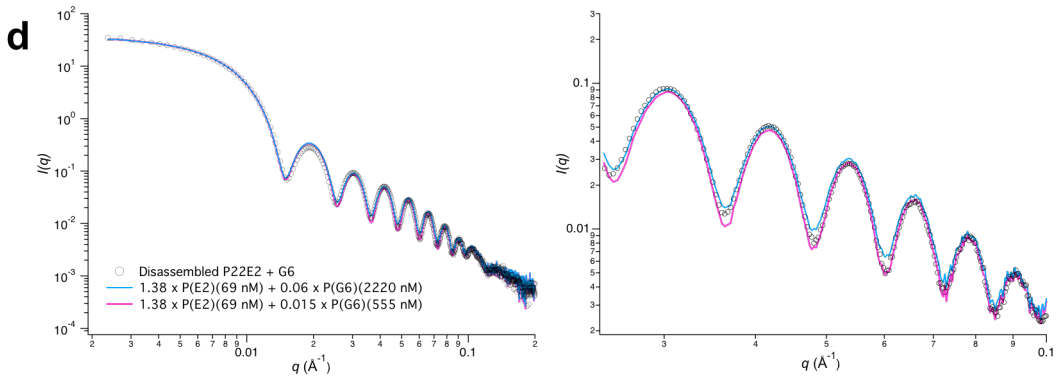

Supplementary Figure S12. (continued). d, At scaling factor f_{G6} = 0.015 (magenta), the calculated intensity of the peak minimum at q = 0.06 and peak maxima at q = 0.066 matched with the measured profile better than f_{G6} = 0.035, while the intensity of other peaks did not match well. At scaling factor f_{G6} = 0.06 (cyan), the calculated intensity of the peak maxima at q = 0.03 and 0.042 matched with the measured profile better than f_{G6} = 0.035, while the intensity of other peaks did not match well. Either below f_{G6} = 0.015 or above f_{G6} = 0.035, all peaks in the calculated profile did not match the measured profile. Therefore, f_{G6} = 0.015 and 0.06 were determined to be the lower and upper limits of the scaling factor, respectively, which correspond to a G6/P22-E2 ratio of 8.0 and 32.1.

Quantification using amino acid analysis

Because PAMAM dendrimers are constructed through amide bonds, a quantitative amino acid analysis technique was utilized to determine the concentrations of G6 and P22 VLPs in superlattices. First, samples containing only G6 dendrimer of different concentrations were treated and measured through the same procedure as other protein samples. An intense peak, which was not observed in amino acids standards and a P22 VLP only sample, was detected slightly after an elution time corresponding to the phenylalanine peak of amino acid standards. There was linear correlation between concentration of G6 dendrimer and area of the peak. Thus, the peak was attributed to a hydrolyzed compound of G6 and used to quantify the concentration of G6 in the samples of P22VLPs with G6. A standard curve of G6 dendrimer concentration was generated from triplicate measurements of known concentrations of G6 (500, 2000 and 5000 nM) mixed with amino acids standards (Supplementary Figure S13). The samples of P22-E2 assembly with ordered superlattice structure (prepared at I = 206 mM) and amorphous structure (prepared at I = 41.1 mM) were analyzed to obtain the concentrations of G6 and P22-E2 in each

sample. The average of G6 / P22-E2 VLP ratio of the superlattice sample was 25.4 ± 4.6, whereas that of the amorphous sample was 52.6 ± 7.5, indicating that the amorphous assembly incorporates twice as much G6 dendrimer as the superlattice assembly.

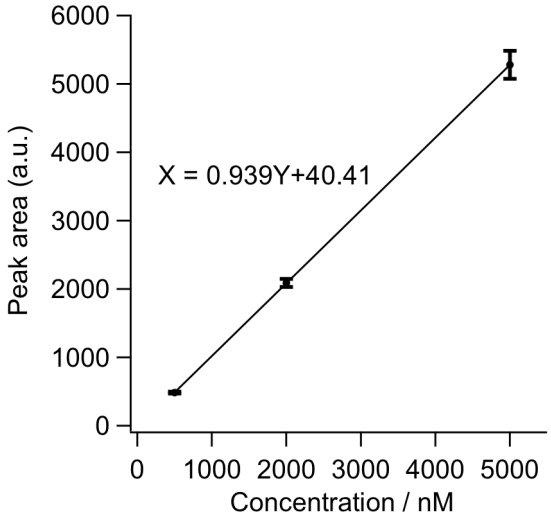

Supplementary Figure S13. Plot of concentration of G6 *versus* peak area detected with reverse phase HPLC after acid hydrolysis.

Supplementary Table S5. The G6 / P22-E2 ratios in the assembly samples with superlattice and amorphous structures determined by amino acid analysis.

Sample	G6 / P22-E2
Superlattice sample (assembled at I = 206 mM)	25.4 ± 4.6
Amorphous sample (assembled at I = 41.1 mM)	52.6 ± 7.5

Section 10. Assessment of P22-E2 VLP assembly with various dendrimer / VLP ratios

P22-E2 VLPs were mixed with various amounts of G6 dendrimer at I = 206 mM (sodium phosphate 50 mM, sodium chloride 100 mM, pH 7.0). The hydrodynamic diameter of particles in each sample solution was analyzed by DLS 30 minutes after adding dendrimer (Supplementary Figure S14). The hydrodynamic diameter remained nearly identical to mono-dispersed P22-E2 VLPs until G6/VLP = 10. A small population of higher order assembly (> 1 μm) was observed at G6/VLP = 20. Large assembly became dominant at G6/VLP = 30 suggesting an excess of 20 – 30 G6 dendrimers per VLP is necessary to mediate P22-E2 assembly into the bulk. This data is consistent with the result in the Section 9, which suggests that about 20 G6 dendrimers per VLP are incorporated in the ordered lattices.

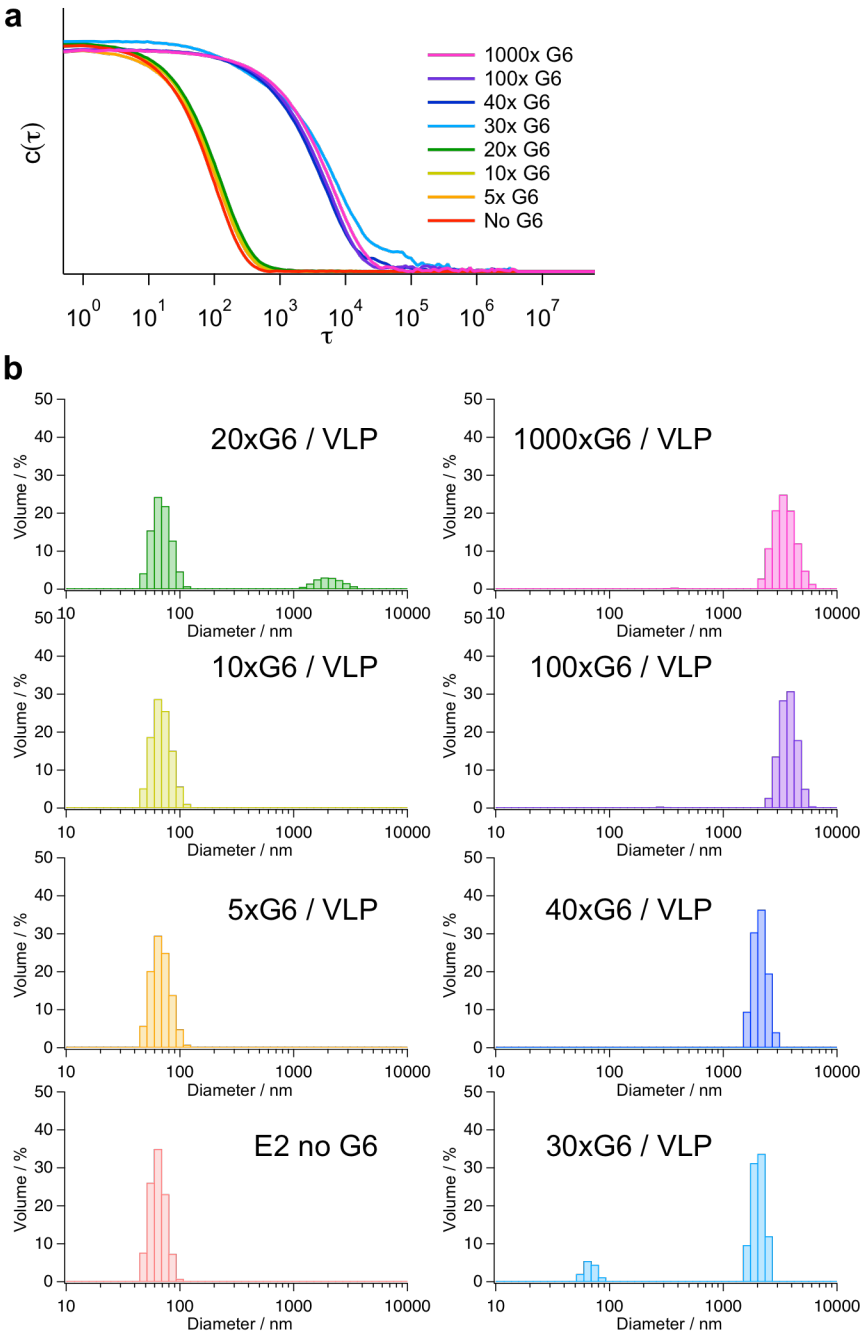

Supplementary Figure S14. (a) Correlation functions and (b) corresponding volume-averaged hydrodynamic diameter distributions of P22-E2 mixed with various amount of G6 per VLP. Drastic increase in particle size was observed at G6/VLP = 30.

Section 11. Characterization of P22-E2-KivD and P22-E2-AdhA

P22-E2-KivD and P22-E2-AdhA VLPs were first analyzed by sodium dodecyl sulfate polyacrylamide gel electrophoresis (SDS-PAGE) and TEM (Supplementary Figure S15). SDS-PAGE indicates that KivD and AdhA are incorporated in the VLPs. Both P22-E2-KivD and P22-E2-AdhA VLPs showed cage-like morphologies of approximately 55 nm diameter that were indistinguishable from P22-E2 VLPs (see Supplementary Figure S1). This suggests that

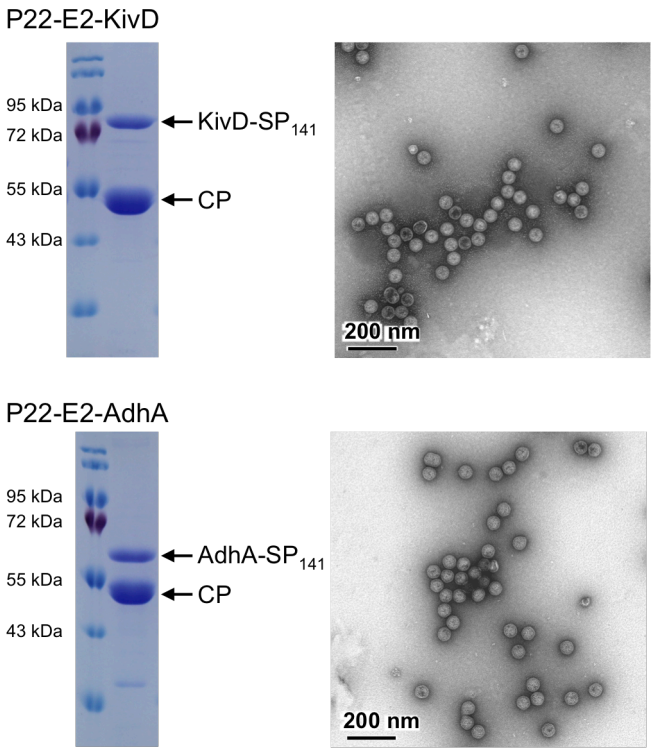

Supplementary Figure S15. SDS-PAGE (left) and TEM images (right) of P22-E2-KivD and P22-E2-AdhA. SDS-PAGE of P22-E2-KivD showed bands corresponding to KivD-SP_{141} (theoretical Mw = 79.7 KDa) and CP-E2 (theoretical Mw = 48.3 KDa). P22-E2-AdhA showed bands corresponding to AdhA-SP_{141} (theoretical Mw = 54.7 KDa) and CP-E2. TEM images of the VLPs exhibited cage-like morphologies of approximately 55 nm diameter.

encapsulation of the enzymes (either KivD or AdhA) as fusion proteins with SP_{141} do not disrupt the assembly of the CP and enzyme-SP_{141} into the VLP. Molecular weight analysis of the P22-E2-KivD and P22-E2-AdhA VLPs with SEC-MALS (Supplementary Table S6) revealed that 127.1±1.4 KivD and 236.2±1.3 AdhA are encapsulated per P22-E2 VLP on average. Because the diameter of the interior cavity of P22 VLP, where the enzymes are encapsulated, is approximately 48 nm, the volume of the cavity is 58,000 nm^3 per VLP. Thus, the number of enzymes per VLP corresponds to a local enzyme concentration in the VLP cavity of 3.64 mM (290 mg/cm^3) for KivD and 6.77 mM (370 mg/cm^3) for AdhA.

Supplementary Table S6. Molecular weights (Mw) of enzyme encapsulated VLPs, and the number of encapsulated enzyme-SP_{141} per capsid, which is calculated based on the Mw of VLPs.

	P22-E2-KivD	P22-E2-AdhA
Measured Mw of VLP	30.41 ± 0.11 MDa	33.20 ± 0.07 MDa
Theoretical Mw of CP subunit	48.29 kDa	48.29 kDa
Theoretical Mw of capsid	20.28 MDa	20.28 MDa
Theoretical Mw of Enzyme-SP_{141}	79.69 kDa	54.69 kDa
Enzyme-SP_{141} / capsid	127.1 ± 1.4	236.2 ± 1.3

Enzymatic activity of individual P22-E2-KivD and P22-E2-AdhA VLPs was measured as described in the Method section. A Michaelis-Menten kinetic model was applied to determine k_{cat} and K_M of each VLP (Supplementary Figure S16). The values of k_{cat} and K_M of P22-E2-KivD were 82.7 (sec^{-1}) and 4.25 (mM), and those of P22-E2-AdhA were 23.4 (sec^{-1}) and 27.0 (mM), respectively. The observed enzymatic activities of P22-E2-KivD and P22-E2-AdhA are comparable to the reported activity values of KivD and AdhA[11-12].

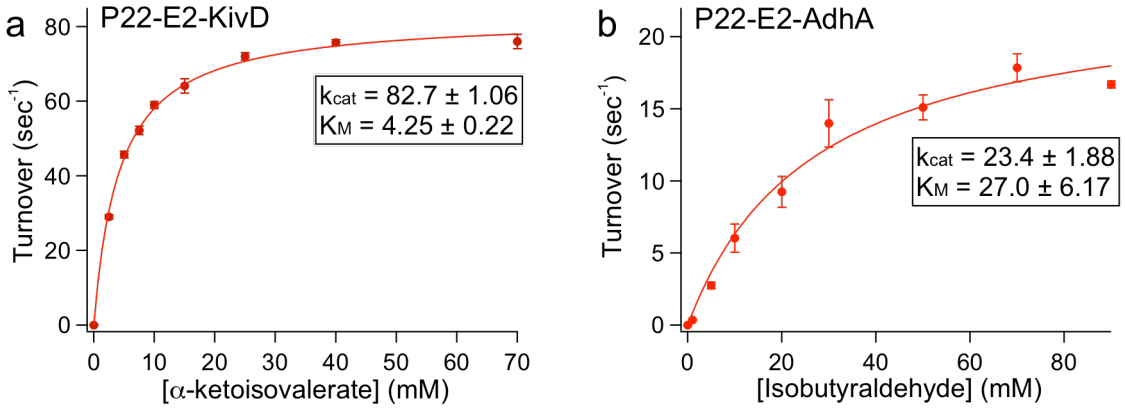

Supplementary Figure S16. Plots of initial turnover against substrate concentration to assess activity of **(a)** P22-E2 KivD and **(b)** P22-E2 AdhA. Values of k_{cat} and K_M were determined by using a Michaelis-Menten kinetic model.

Section 12. Investigation of enzyme encapsulated VLPs + G6 assemblies

The higher order assembly of P22-E2-KivD and P22-E2-AdhA with G6 at varying ionic strengths (*I*) was investigated by turbidity assessments (Supplementary Figure S17). The assembly propensity and I_T was the same regardless of the type of cargo encapsulated inside of VLPs, suggesting that the assembly depends on interactions between the exterior surface of VLPs and G6 and is independent of interior of the VLPs.

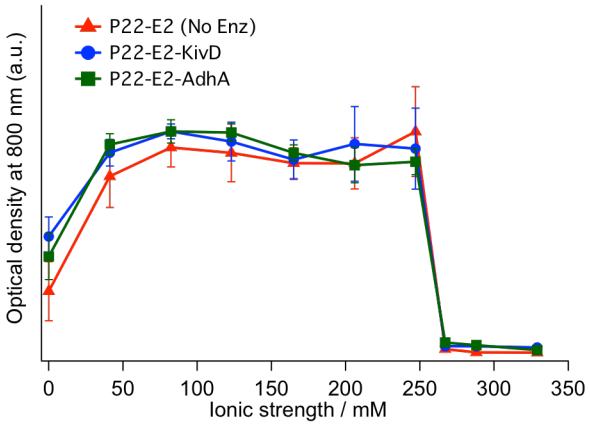

Supplementary Figure S17. Assembly of P22-E2 VLP and those loaded with KivD or AdhA under a range of ionic strengths (*I*) was assessed by monitoring light scattering at 800 nm. A rapid increase in optical density due to formation of higher order assembly was observed upon addition of G6 PAMAM dendrimer to both wtP22 and P22-E2 under *I* = 0 – 247 mM. Threshold ionic strength (I_T) was same regardless of type of interior cargo molecules.

The distribution of the two populations of VLPs (*i.e*. P22-E2-KivD and P22-E2-AdhA) in co-assembled bulk materials was investigated with confocal fluorescence microscopy. P22-E2-KivD labeled with DyLight405 and P22-E2-AdhA labeled with Texas Red were mixed at a 1:1 molar ratio, co-assembled with G6 dendrimer into bulk materials at *I* = 206 mM, and then observed with confocal fluorescence microscopy. The images clearly suggest that P22-E2-KivD and P22-E2-AdhA are homogeneously distributed throughout the assembled bulk material (Supplementary Figure S18). This result also suggests that higher order assembly of VLPs is independent of the types of interior cargo molecules.

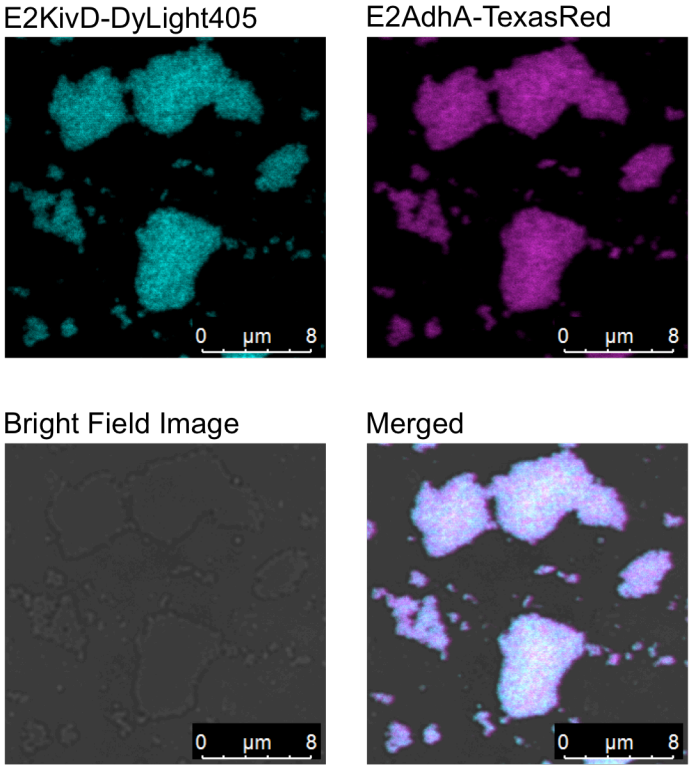

Supplementary Figure S18. Confocal fluorescence microscope images of higher order assemblies composed of P22-E2-KivD and P22-E2-AdhA. The both types of VLPs distribute homogeneously over the assembled materials.

Section 13. SAXS analysis of enzyme encapsulated VLPs + G6 assemblies

P22-E2-AdhA, P22-E2-KivD and the mixture of the two VLPs were each mixed with G6 dendrimer in buffers with various ionic strengths and the structures of the arrays were investigated using SAXS. In all three cases, more prominent SAXS scattering peaks (q = 0.012, 0.020, 0.032, 0.043), which are attributed to an FCC structure, were observed with increasing ionic strength up to a threshold ionic strength (I = 247 mM) and the VLPs no longer assembled beyond the threshold (Supplementary Figure S19). The trend of ionic strength dependent assembly and obtained structure of the superlattices are the same as P22-E2 without enzyme.

In the FCC lattice with lattice parameter a = 87 nm, the volume of a unit cell is 658,503 nm^3. There are four VLPs per unit cell and the volume of the interior cavity is 58,000 nm^3. Thus, the total volume of the cavity per unit cell is 232,000 nm^3, which occupies about 35% of the total volume of the unit cell. As the local concentration of the enzymes in the VLP cavity were estimated to be ~ 300 mg/cm^3 (see the Supplementary Information Section 11), the enzyme concentration within the superlattice is calculated to be ~ 100 mg/cm^3.

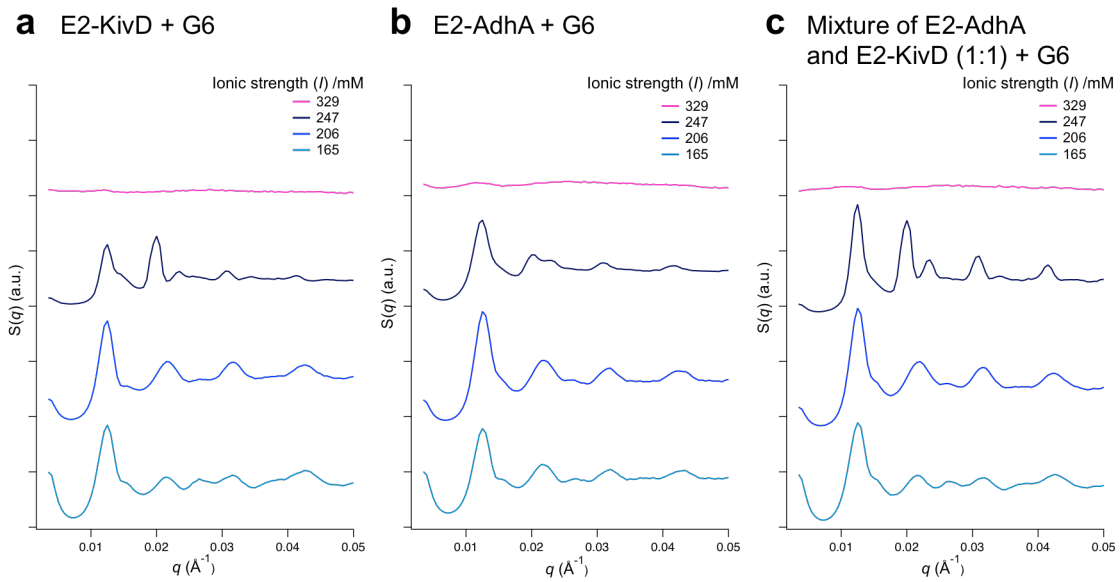

Supplementary Figure S19. Structure of **(a)** P22-E2-KivD, **(b)** P22-E2-AdhA, **(c)** a 1:1 ratio mixture of P22-E2-KivD and P22-E2-AdhA assembled with G6 in buffer solutions with various ionic strengths investigated by SAXS. (Plots are vertically offset for clarity) More prominent scattering peaks due to long-range order of assembled VLPs were observed with increasing ionic strength up to I = 247 mM. Above the threshold ionic strength, the VLPs did not assemble. The peak positions and trend of ionic strength dependence on the assembly are the same as those without cargo enzymes.

Section 14. Additional data for catalytic activity assays

Because the nanoreactor superlattices are bulk materials, they can be readily condensed *via* settling down or gentle centrifugation followed by re-suspension (Supplementary Figure S20) into smaller volumes of solution. The ease of handling nanoreactor superlattices also leads to a method for simple separation from the product for reuse (Supporting Information Section 15).

Production of isobutyraldehyde (shared intermediate between KivD and AdhA) and isobutanol (final product) was assessed with GC-MS. The volatile reaction products were detected by electron ionization mass spectrometry (EI-MS; Agilent 5973inert), which monitored

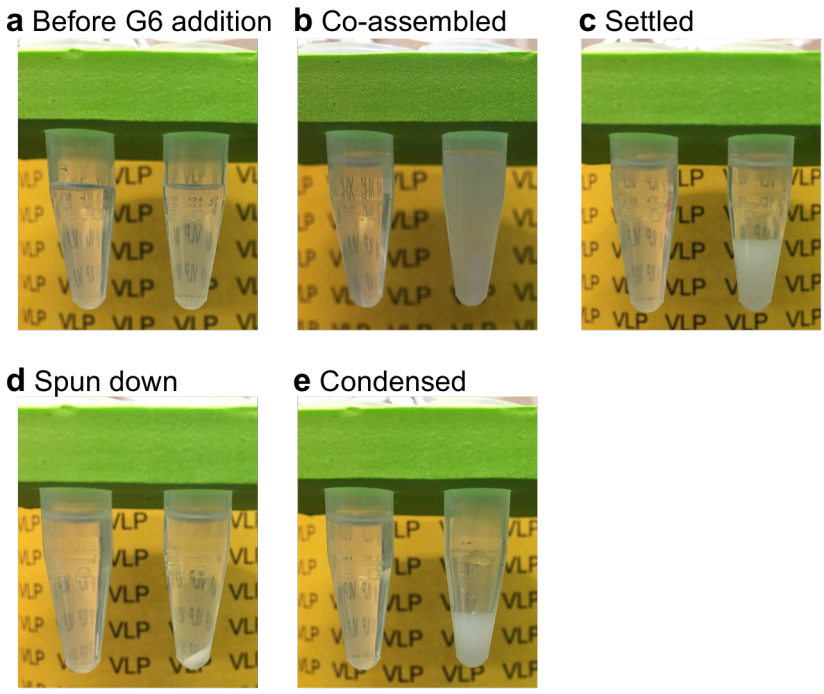

Supplementary Figure S20. Pictures of P22 VLP assembled into superlattices followed by pelleting of the material *via* low speed centrifugation. **(a)** P22 VLPs dispersed in solution before addition of G6 dendrimer. **(b)** The solution became turbid immediately after addition of G6 dendrimer (right), indicating assembly of P22 VLPs into superlattices. The control solution (left), in which phosphate buffer supplemented with methanol at a ratio of 4:1 (vol/vol) were added, stayed clear, indicating VLPs were freely dispersed in solution. **(c)** The assembled superlattices settled down to the bottom within 2h after adding G6 dendrimer (right). The control solution stayed clear and no precipitate was observed (left). **(d)** The superlattices were pelleted down by centrifugation at 5000 g for 3 min (right). There was no visible precipitate in the control solution after the centrifugation (left). **(e)** The supernatant was removed and the superlattice pellet was re-suspended into small volume (10% of initial volume) of phosphate buffer.

m/z = 43, 72, and 74 in select ion monitoring (SIM) mode. Elution time of isobutyraldehyde and isobutanol were confirmed as around 8.2 min and 10.4 min, respectively, by measuring isobutyraldehyde and isobutanol standards individually. Extracted ion chromatograms of m/z = 43, corresponds to isopropyl fragment ions of both isobutyraldehyde and isobutanol, are shown in Supplementary Figure S21. The result shows that production of isobutanol is significantly accelerated in the condensed co-assembly of VLP nanoreactors in comparison with non-condensed co-assembly and free VLP nanoreactors.

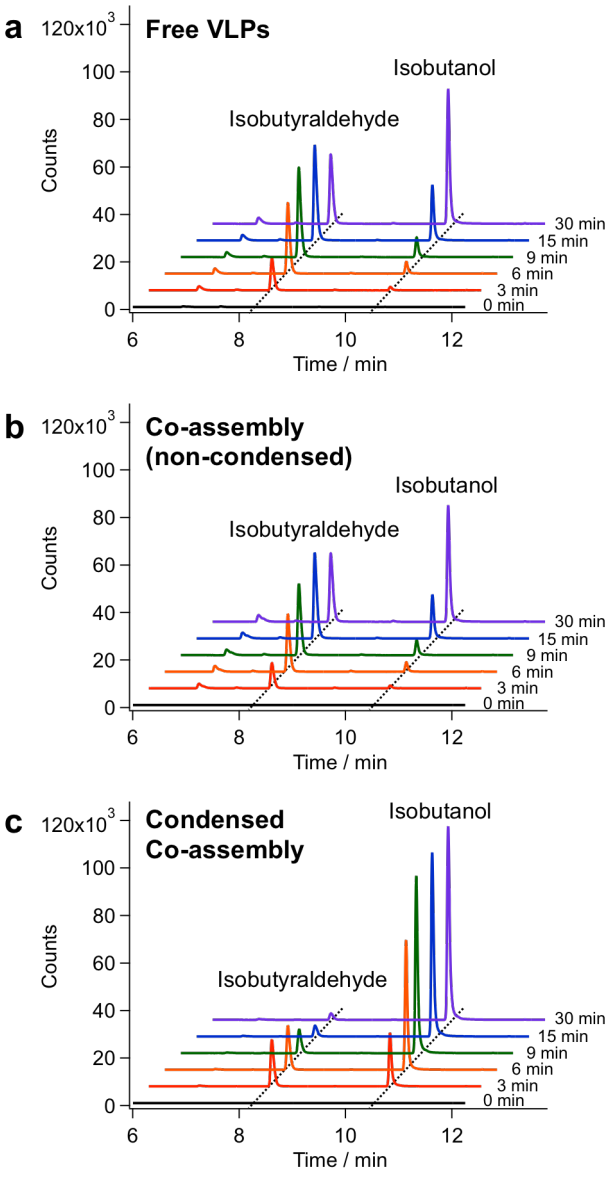

Supplementary Figure S21. GC-MS analysis of isobutyraldehyde and isobutanol productions in nanoreactor superlattices composed of P22-E2-KivD and P22-E2-AdhA VLPs and corresponding free nanoreactors. Extracted ion chromatogram of m/z = 43 over the time of catalytic reaction are shown to monitor production of isobutyraldehyde and isobutanol. Mixtures of **(a)** free VLPs and **(b)** non-condensed superlattices showed similar profiles of isobutyraldehyde (intermediate) and isobutanol (final product) production, whereas **(c)** condensed superlattices sample showed significantly accelerated progress of the two-step catalytic reaction.

Catalytic activity of condensed co-assemblies of VLP nanoreactors was also compared with the mixture of the same concentration of free VLPs (*i.e.* 10 times higher concentration than free VLPs shown in Figure 5b) by monitoring NADH depletion (Supplementary Figure S22). Catalytic activity of condensed nanoreactor superlattices was nearly identical to the free VLPs with same concentration. This is consistent with the result shown in Figure 5b comparing the activity between free and assembled VLPs under non-condensed conditions. This further demonstrates that the assembled bulk materials retain their catalytic activity comparable to individual nanoreactor VLPs free in solution regardless of concentration of nanoreactor VLPs.

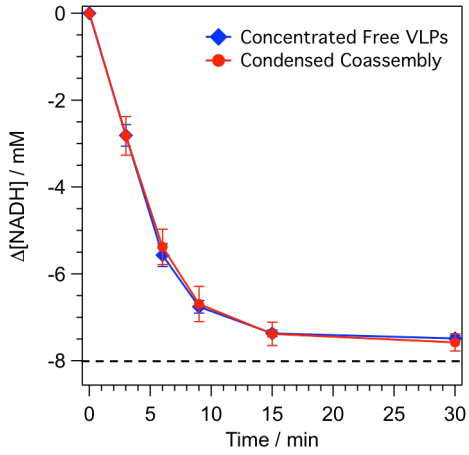

Supplementary Figure S22. Depletion of NADH was monitored to compare catalytic activity of condensed co-assembly of VLP nanoreactors with mixture of same concentration of free VLPs. The NADH depletion profiles between these two conditions are nearly identical, indicating that efficiency of the two-step catalytic conversion from α-ketoisovalerate to isobutanol is not diminished when VLP nanoreactors are assembled into bulk materials. The dotted line indicates 100% conversion of supplied substrate to the final product.

Section 15. Reusability of nanoreactor superlattices

The nanoreactor superlattices were subjected to the catalytic activity assay three times to evaluate their robustness and reusability as catalytic materials. After each cycle of activity assay, the superlattices were pelleted down *via* centrifugation at 5,000 g for 3 min and isolated from the product. The catalytic activity of the superlattices was evaluated by NADH depletion, which is well correlated with production of isobutanol as shown in Figure 5. Depletion of NADH followed nearly the same trends for each of the three cycles, indicating that the nanoreactor superlattices maintain their catalytic activity through at least three cycles of turnover and recovery (Supplementary Figure S23).

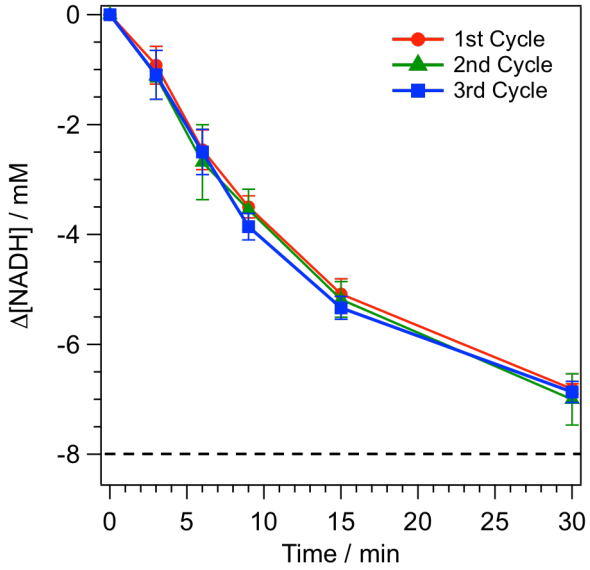

Supplementary Figure S23. Depletion of NADH was monitored to evaluate catalytic activity of nanoreactor superlattices over three cycles of the two-step catalytic reaction. The NADH depletion profiles followed nearly identical trends, indicating that the superlattices maintain their activity over three cycles of the catalytic reactions. The dotted line indicates 100% conversion of supplied substrate to the final product.

Section 16. References

(1) Servid, A.; Jordan, P.; O'Neil, A.; Prevelige, P.; Douglas, T., Location of the Bacteriophage P22 Coat Protein C-Terminus Provides Opportunities for the Design of Capsid-Based Materials. *Biomacromolecules* **2013,** *14*, 2989-2995.

(2) Li, T.; Senesi, A. J.; Lee, B., Small Angle X-Ray Scattering for Nanoparticle Research. *Chem. Rev.* **2016,** *116*, 11128-11180.

(3) Hosemann, R.; Vogel, W.; Weick, D.; Baltacalleja, F. J., Novel Aspects of the Real Paracrystal. *Acta Crystallogr. Sect. A* **1981,** *37*, 85-91.

(4) Matsuoka, H.; Tanaka, H.; Hashimoto, T.; Ise, N., Elastic Scattering from Cubic Lattice Systems with Paracrystalline Distortion. *Phys. Rev. B* **1987,** *36*, 1754-1765.

(5) Matsuoka, H.; Tanaka, H.; Iizuka, N.; Hashimoto, T.; Ise, N., Elastic Scattering from Cubic Lattice Systems with Paracrystalline Distortion Ii. *Phys. Rev. B* **1990,** *41*, 3854-3856.

(6) O'Brien, M. N.; Girard, M.; Lin, H. X.; Millan, J. A.; Olvera de la Cruz, M.; Lee, B.; Mirkin, C. A., Exploring the Zone of Anisotropy and Broken Symmetries in DNA-Mediated Nanoparticle Crystallization. *Proc. Natl. Acad. Sci. USA* **2016,** *113*, 10485-10490.

(7) Exner, A.; Rosenfeldt, S.; Fischer, S.; Lindner, P.; Forster, S., Defect Accommodation in Nanostructured Soft Crystals. *Nanoscale* **2014,** *6*, 1635-1645.

(8) Glatter, O., The Interpretation of Real-Space Information from Small-Angle Scattering Experiments. *J. Appl. Crystallogr.* **1979,** *12*, 166-175.

(9) Hummer, D. R.; Heaney, P. J.; Post, J. E., *In Situ* Observations of Particle Size Evolution During the Hydrothermal Crystallization of TiO_2 a Time-Resolved Synchrotron SAXS and WAXS Study. *J. Cryst. Growth* **2012,** *344*, 51-58.

(10) Langford, J. I.; Wilson, A., Scherrer after Sixty Years: A Survey and Some New Results in the Determination of Crystallite Size. *J. Appl. Crystallogr.* **1978,** *11*, 102-113.

(11) de la Plaza, M.; de Palencia, P. F.; Pelaez, C.; Requena, T., Biochemical and Molecular Characterization of Alpha-Ketoisovalerate Decarboxylase, an Enzyme Involved in the Formation of Aldehydes from Amino Acids by *Lactococcus Lactis*. *FEMS Microbiol. Lett.* **2004,** *238*, 367-374.

(12) Liu, X.; Bastian, S.; Snow, C. D.; Brustad, E. M.; Saleski, T. E.; Xu, J.-H.; Meinhold, P.; Arnold, F. H., Structure-Guided Engineering of *Lactococcus Lactis* Alcohol Dehydrogenase LlAdhA for Improved Conversion of Isobutyraldehyde to Isobutanol. *J. Biotechnol.* **2012,** *164*, 188-195.